

NUMERICAL INVESTIGATION OF A JET FLOW WITH A HATCH AND AN OPENING

A Thesis by

Mrinal V. Nagrecha

Bachelor of Science, Wichita State University, 2009

Submitted to the Department of Aerospace Engineering
and the faculty of the Graduate School of
Wichita State University
in partial fulfillment of
the requirements for the degree of
Master of Science

December 2011

© Copyright 2011 Mrinal Nagrecha

All Rights Reserved

NUMERICAL INVESTIGATION OF A JET FLOW WITH A HATCH AND AN OPENING

The following faculty members have examined the final copy of this thesis/dissertation for form and content, and recommend that it be accepted in partial fulfillment of the requirement for the degree of Master of Science with a major in Aerospace Engineering.

Klaus A. Hoffmann, Committee Chair

Roy Myose, Committee Member

Ikram Ahmed, Committee Member

DEDICATION

To my family,
for all the love and money they showered upon me

ACKNOWLEDGMENTS

I would like to thank my advisor, Dr. Klaus Hoffmann, for his time and patience. His kind demeanor and guiding hand were an integral part of my success. My friends Alex Clayton and Patrick Rinker deserve recognition for helping me realize when to stop and take a look at the big picture, but most importantly, Nghi Lam, deserves my thanks for keeping me grounded and focused.

Additional thanks go to Shoeb, Nilou, Paul, and Armin for their guidance.

ABSTRACT

The goal of this project was to establish a datum for acoustics generated in an exhaust flow from a jet pipe, due to the presence of an opening with a hatch at an angle, by using the Computational Fluid Dynamics (CFD) tool FLUENT. After validating the geometry using a supersonic case employing a fully expanded jet, a secondary supersonic test case was produced to compare results with the former using a Detached Eddy Simulation with Spalart-Allmaras (DES-SA) scheme. Two subsonic cases using the same boundary conditions (BCs) were then computed using a Large Eddy Simulation (LES) turbulence model in order to solve for flow-field data and Sound Pressure Level (SPL) of the given geometry. Focus was given to the region around the opening, and the computed pressure data was stored in three regions: above the opening, under the opening, and past the opening. Pressure contours in the region around the hatch were captured well and shown to be consistent between the two geometries employed for the domain of solution. Results concluded that using the smaller domain of solution maintained resolution quality while decreasing overall computation time tremendously.

TABLE OF CONTENTS

Chapter	Page
1. INTRODUCTION	1
1.1 Turbulent Boundary Layers and Wall Pressure Fluctuations	1
1.2 Jet Flow	14
2. MODEL DESCRIPTION	25
2.1 Generic Geometry	25
2.2 Determining Domain of Solution, and Boundary Conditions	26
3. MODEL VALIDATION	28
3.1 Model Geometry, Domain of Solution, and Boundary Conditions	28
3.2 Meshing	29
3.3 Results	30
4. TEST CASE VERSIONS	33
4.1 Test Case Version 1	33
4.1.1 Geometry, Domain of Solution, and Boundary Conditions	33
4.1.2 Meshing	33
4.1.3 Solution Procedure	34
4.1.4 Results	35
4.2 Test Case Version 2	39
4.2.1 Geometry, Domain of Solution, and Boundary Conditions	39
4.2.2 Meshing	40
4.2.3 Solution Procedure	41
4.2.4 Results	42
4.3 Final Version—Unstructured Mesh	51
4.3.1 Geometry, Domain of Solution, and Boundary Conditions	51
4.3.2 Meshing	52
4.5.3 Solution Procedure	53
4.3.4 Results	53
5. CONCLUSIONS	63
REFERENCES	65

LIST OF TABLES

Table		Page
1.	Version 1 Cell Distribution—Volume	34
2.	Version 1 Cell Distribution—Skewness Range	34
3.	Version 2 Cell Distribution—Volume	40
4.	Version 2 Cell Distribution—Skewness Range	41
5.	Final Version Cell Distribution—Volume	52
6.	Final Version Cell Distribution—Skewness Range	52

LIST OF FIGURES

Figure	Page
1. Isometric view of jet pipe	25
2. Front view of jet pipe	25
3. Opening and hatch with respect to jet exhaust pipe.....	26
4. Validation case: Boundary layer	29
5. Validation case: Fully expanded jet mesh	30
6. Validation case: Centerline velocity	31
7. Validation case: Contours of velocity magnitude.....	31
8. Validation case: Velocity profiles.....	32
9. Version 1: Unstructured tetrahedral mesh	33
10. Version 1: Pressure contours at 0.1 s	35
11. Version 1: Centerline pressure at 0.1 s	36
12. Version 1: Contours of velocity magnitude at 0.1 s.....	37
13. Version 1: Centerline velocity at 0.1 s.....	37
14. Version 1: X-velocity iso-surface at 0.1 s.....	38
15. Version 1: X-velocity profiles at (a) $x/D = 2.5$, (b) $x/D = 2.667$, and (c) $x/D = 2.833$	38
16. Version 1: TVR with mesh at 0.1 s.....	39
17. Version 2: Unstructured mesh around hatch and opening	40
18. Version 2: Contours of static pressure at 0.05 s.....	42
19. Version 2: Contours of static pressure at 0.1 s.....	43
20. Version 2: Velocity profile at 0.05 s.....	44
21. Version 2: Velocity profile at 0.1 s.....	44

LIST OF FIGURES (continued)

Figure	Page
22. Version 2: X-velocity iso-surface at 0.05 s.....	45
23. Version 2: X-velocity iso-surface at 0.1 s.....	46
24. Version 2: X-velocity profiles at (a) $x/D = 2.5$, (b) $x/D = 2.667$, and (c) $x/D = 2.833$	46
25. Version 2: Subgrid turbulent viscosity at 0.05 s.....	47
26. Version 2: Subgrid turbulent viscosity at 0.1 s.....	47
27. Version 2: Pressure monitors around opening and hatch.....	48
28. Version 2: SPL “on top” of hatch	49
29. Version 2: SPL “below” hatch.....	49
30. Version 2: SPL “in front” of hatch	50
31. Final Version: Domain of solution	51
32. Final Version: Contour of static pressure at 0.1 s.....	54
33. Comparison of centerline pressure at 0.1 s	55
34. Final Version: Velocity magnitude at 0.1 s	56
35. Final Version: X-velocity iso-surface at 0.1 s	57
36. Final Version: X-velocity profiles at (a) $x/D = 2.5$, (b) $x/D = 2.667$, and (c) $x/D = 2.833$	57
37. Comparison of centerline velocity magnitude at 0.1 s.....	58
38. Final Version: Subgrid turbulence viscosity at 0.1 s	59
39. Final Version: Pressure monitors around opening and hatch	60
40. Final Version: SPL “on top” of hatch.....	61
41. Final Version: SPL “below” hatch.....	61

LIST OF FIGURES (continued)

Figure	Page
42. Final Version: SPL “in front” of hatch	62

LIST OF ABBREVIATIONS

2D	Two-Dimensional
3D	Three-Dimensional
BC	Boundary Condition
BL	Boundary Layer
CDS	Central Differencing Scheme
CFD	Computational Fluid Dynamics
CPU	Central Processing Unit
DES	Detached Eddy Simulation
DES-SA	Detached Eddy Simulation with Spalart-Allmaras
DDES	Delayed Detached Eddy Simulation
DDES-SA	Delayed Detached Eddy Simulation with Spalart-Allmaras
DNS	Direct Numerical Simulation
FPS	Frequency Power Spectrum
HiPeCC	High Performance Computing Center
LDA	Laser Doppler Anemometer
LES	Large Eddy Simulation
LR	LES Region
NPR	Nozzle Pressure Ratio
NS	Navier-Stokes
NSE	Navier Stokes Equation
OASPL	Overall Sound Pressure Level
PIV	Particle Image Velocimetry
RANS	Reynolds-Averaged Navier-Stokes

LIST OF ABBREVIATIONS (continued)

RANS-SA	Reynolds Average Navier-Stokes with Spalart-Allmaras
RMS	Root Mean Square
RR	RANS Region
SA	Spalart-Allmaras
SLSE	Spectral Linear Stochastic Estimation
SGS	Subgrid Scale
SPIV	Stereo Particle Image Velocimetry
SPL	Sound Pressure Level
SST	Shear Stress Transport
TBL	Turbulent Boundary Layer
TKE	Turbulent Kinetic Energy
TVD	Total Variation Diminishing
TVR	Turbulence Viscosity Ratio
UC	University of Connecticut

LIST OF VARIABLES

κ	Turbulent Kinetic Energy
ρ	Density
μ	Dynamic Viscosity
μ_t	Turbulent Eddy Viscosity
D	Diameter
I	Turbulent Intensity
p	Unsteady Pressure (Mean Zero) Due to Turbulence

CHAPTER 1

INTRODUCTION

Computational Fluid Dynamics (CFD) has helped researchers make great progress in various fields of engineering. Numerous applications, whether working hypotheses or examples readily seen in nature, have been modeled and simulated using various numerical techniques, and have been validated by analytic techniques as well as extensive experimental data provided through testing. Over the years, CFD has proven to be an inexpensive alternative to experimental testing due to the ever-growing number of models and techniques being validated for different conditions and test cases observed. Outstanding growth in the computer hardware industry in the last twenty years has also been a large factor in making CFD such a viable tool. Central Processing Unit (CPU) speeds and hard-drive capacity have grown exponentially over the last two decades, allowing for complex processes to be executed and vast amounts of data to be stored with relative ease for a nominal fee.

The literature survey in this thesis will focus on the advancements made in the field of Turbulent Boundary Layer (TBL) pressure fluctuation using numerical simulations, i.e., Reynolds-Averaged Navier-Stokes (RANS) equation, Large-Eddy Simulation (LES), as well as hybrid techniques such as Detached-Eddy Simulation (DES) and Delayed-Detached-Eddy Simulation (DDES), which can be used in conjunction with more advanced turbulence models. It will also examine cavities/openings in a flow and the overall effects when coupled with an angled cover. Jet flows will also be reviewed.

1.1 Turbulent Boundary Layers and Wall Pressure Fluctuations

In 1995, Bull [1] pointed out the astounding groundwork laid by E. J. Richards due to his research in fluid mechanics during the late 1950s. This proved to be the foundation for future

studies in the field of (but not limited to) pressure fluctuation in a TBL for the next forty years. He attributed the motivation for generating research in the understanding of the turbulent boundary layer to the desire for understanding the creation of a pressure field generated by it and defining its properties. His efforts have provided valuable insights to numerous problems faced by modern engineers. Bull also referenced Willmarth's [2] assessment in 1975, which reviewed some of the major milestones in the early 1960s and proceeded to discuss the improvements made since then.

A noteworthy improvement in the study of wall-pressure fluctuations would be the Kraichnan-Phillips theorem. Using Navier-Stokes equations for the basis of their analysis, Kraichnan and Phillips showed that at given conditions, the wavenumber-frequency spectrum of a flow field is zero at a wavenumber of zero. This fact is irrespective of the frequency of the pressure field. Further modifications were made to the Kraichnan-Phillips theorem as more research was conducted on the topic. It was realized by Ffowcs-Williams [3] that the theory did not hold true when the Mach number of the flow was not zero. Ffowcs-Williams noted that supersonic phase velocities were observed in a pressure field's spectral components and may be subject to the effects of compressibility. These components were realized to be acoustic waves. Bull [1] also pointed out the improvements made in frequency-spectral scaling, indulging in applications of the Kraichnan-Phillips theorem in low-frequency scenarios.

It is also interesting to look at structural responses in different applications due to the presence of an excited turbulent boundary layer. Birgersson [4] compiled 17 different cases where structural responses were an interesting phenomenon to consider. He deemed them important due to the influence of aerodynamic noise causing higher internal noise levels and external noise emissions to increase. Hence, the importance of understanding turbulent flow of

water in long cylindrical pipes, acoustics in automobiles, panel vibrations in aircraft, and other various applications were given time and attention. Solving the aforementioned problems can be quite challenging because analytic solutions, if available, cannot accurately predict results. This statement is especially true in cases where interaction between the body and its surroundings creates a non-linear problem. Thus, experiments are relied upon to help further understanding and provide raw data for future numerical analysis. Experiments conducted recently benefit from the availability of extremely precise equipment like anemometers, vibrometers, and laser velocimeters; better-designed/functioning subsonic, transonic, and supersonic wind tunnels with more accurate accelerometers and pressure probes/transducers; and more sensitive load cells. The improvement in technology over the years has made experimental testing quicker and more accurate.

In 1962, Willmarth and Wooldridge [5] conducted experiments measuring pressure fluctuations on the wall beneath a thick TBL. This exercise yielded tremendous amounts of data, including, but not limited to, mean-square pressure, space-time, and spatial correlation of pressure. Willmarth and Wooldridge also stated the importance of the influence of turbulence in a boundary layer. On rigid surfaces, it is the source of aerodynamic noise, and on yielding surfaces, it causes structural vibrations; neither influence is positive on the body in question. In general, obtaining a clear picture of the pressure fluctuations of the turbulent boundary layer will provide greater detail of its structure. Even though the first few experiments on turbulent flows focused on isotropic turbulence, it wasn't very long until researchers realized the importance and difficulty in accurately representing pressure fluctuations in anisotropic turbulence conditions. Literature at the time pointed to the interaction of turbulence with the mean wall shear to be the primary cause of these pressure fluctuations. It was also thought that the root-mean square

(RMS) of the fluctuations and wall shear stress were of the same order. Experiments conducted at a later time were used to validate the aforementioned assumptions. Since pressure transducers interfered with flows to a certain extent, researchers at the time resorted to hot-wire anemometry to acquire data. Willmarth and Wooldridge, on the other hand, continued using pressure transducers and ensured that they were flush with the surface.

At this point in time, many experiments had been conducted on subsonic/supersonic flows, fully developed flows, and flows beneath a wall jet. The primary result of most of these experiments was the acquisition of a pressure spectrum, along with a space-time correlation for the data. After collecting all available data from the experiments performed and correlating the work, it was concluded that the velocity of pressure fluctuations being convected downstream was approximately eighty percent of the freestream velocity. Decay effects came into play after being convected a few boundary layer thicknesses downstream. Due to the comparatively large size of the pressure transducers with respect to the BL, information on the structure of the wall-pressure fluctuations could not be discerned. Hence, Willmarth and Wooldridge's goal became to acquire greater insight into the structure as well as the cause of these fluctuations—eddies. Their experiment was performed using the facilities available at the University of Michigan.

In order to keep the pressure transducers functioning in perfect condition and reduce fluctuations in data measurement, the transducers as well as input circuitry were kept in an air-tight container. To minimize vibrations, the transducers were held in place with steel mounts filled with sand. Magnetic tapes were used to store and review data. A time delay was incorporated in order to assist with pressure signal correlations, which were measured with a thermocouple. These correlations were acquired by calculating the sums and differences of the signals, and then passed through a band-pass filter before being connected to the thermocouple.

Finally, a dual-beam oscilloscope was used to monitor electrical signals. A very important source of concern was the influence of the sound field in the test section. Anything from the wind-tunnel fan to minute vibrations can influence the data being collected. It was observed that some of the signals produced in the test section were caused by upstream propagation of sound. Understanding the influence of turbulence in the test section C, care must be taken. It was observed that lower frequencies generated the largest energy densities due to wall-pressure fluctuations. Surface roughness can also influence BL turbulence. Results show an increase in the fluctuation of wall shear stress and pressure as well as an increased power spectrum. Willmarth and Wooldridge also noted that the presence of the sun influences wall-pressure fluctuations. It was observed that in the absence of the sun, a very interesting phenomenon occurred—mean-square wall pressure decreased.

The use of titanium tetrachloride to produce smoke caused large-scale oscillations in the streamlines at the contraction region of the tunnel, and its interaction with the test section boundary layer was confirmed. These fluctuations were caused by vorticity, which in turn were the result of the acceleration of density-stratified air produced by heat transfer. A Stanton tube and a Pitot tube were used to acquire measurements for shearing stress, mean-velocity profile, BL thickness, displacement, and momentum thicknesses. When trying to assess the convection speed of eddies, it was observed that the speeds were lower in the high-frequency band than in the lower-frequency band. It was assumed that low-frequency pressure fluctuations cause larger eddies, and high-frequency pressures cause smaller eddies. Therefore, larger eddies had a higher average convection speed than their smaller counterparts. Willmarth and Wooldridge also showed that a higher rate of decay is observed in larger eddies in comparison to smaller eddies. Finally, it was shown that the experimental data corroborated well with predicted data.

In 1965, Willmarth and Roos [6] furthered the work of Willmarth and Wooldridge [5] by examining the structure of the wall pressure field in a TBL. Their objective was to convey the impact of transducer geometry on statistical properties. Using information from previous experiments, they investigated the implementation of even smaller pressure transducers. In doing so, they observed a noticeable increase in the accuracy with which RMS wall pressure had been measured. In fact, other statistical properties also varied with transducer size and shape. It was observed that if the transducer had a linear response to pressure, corrections could be applied to the data derived from it; therefore, comparisons were made between the data acquired from circular transducers of different diameters. Discrepancies were found when compared to the work published by Willmarth and Wooldridge [5], and the methods were corrected and data reevaluated. Due to wear and tear damage in the tunnel, namely leaks, rattles, and loss of turbulence screens, lower-frequency data were observed to have scattering in the spectra. Due to the compromised structure, at higher frequencies, background noise and vibration essentially washed out pertinent TBL pressure field data.

In 1967, Bull [7] performed an experiment measuring the effect of TBL flow on wall-pressure fluctuations. He collected experimental data from wind tunnel testing using a natural transition from laminar to turbulent flow over a smooth wall; RMS pressure, Frequency Power Spectrum (FPS), and space-time correlations at both narrow and broad frequency bands were collected from the experiment. This work showed that a broad band of convection velocities facilitated the structure of wall-pressure fields and was comprised of two prominent wavenumber components: one of a high wavenumber linked to the stress layer and the turbulent motion in it, and the other coupled with large-scale eddy motions in the BL and observed past the stress layer. This latter component was also known for a wavelength twice that of the BL thickness and

causing an independent loss of coherence. Unlike velocity fluctuations, pressure fluctuations were harder to measure at this point in time. Only a few successful experiments were available in cases that employed wake flow and isotropic turbulence. Pressure fluctuations were difficult to measure in experiments without compromising the quality of the flow by introducing equipment. It was often observed that the pressure transducer was too large when compared to the thickness of the boundary layer, which often led to attenuation of pressure signals at higher frequencies. Bull then proceeded to reference work by Kraichnan in 1956–57 on turbulent shear flows. Kraichnan’s theoretical outlook on pressure fluctuations led him to believe that it was the local velocity fluctuations that were the cause of fluctuations in pressure, and the interaction between mean-shear layer and turbulence contributes greatly to the mean-square pressure. Kraichnan also believed that the aforementioned statement may not be true for low wavenumbers.

By then, a few researchers had conducted experimental work in subsonic regimes, and fewer worked with supersonic and water flow cases such as wall jets and pipes with fully developed turbulent flows. Even though the focus of these experiments was on pressure fluctuations in the TBL, wide discrepancies among researchers were observed in subsonic data for RMS pressure fluctuation. Incongruities were also seen in data measuring the nature of convection for wall-pressure fields as well as the frequency spectrum. Keeping this in mind, Bull attempted to reduce his errors by using hardware that would not interfere with the experiment, i.e., by using miniature pressure-sensing elements.

Another objective set by Bull was to investigate the behavior of various wavenumber components and hence have a better understanding of the structure of pressure fields. When considering the pressure scales, it was realized that there were two regions in the boundary layer, each with its own scale—the inner region and the outer region. The inner region was comprised

of the constant stress region, while the outer region had more wake-like tendencies. The objective, as far as scales were considered, was adapted to minimize the dependence of the wall-pressure field on the Reynolds number. This experiment was conducted on a TBL from a natural transition on a polished surface of a subsonic wind tunnel test section at the University of Southampton. To prevent a pressure gradient from developing in the test section, the section diverged in order to compensate for the growth in the BL. Pressure readings were collected using flush wall-mounted piezoelectric transducers.

In 1979, Howe [8] discussed surface shear stresses and how they interacted with the boundary layer in regard to the generation and propagation of acoustic waves. His work showed that sound was not generated by the “dipole” of the surface shear stress, but rather, the dipole governed the propagation of sound. Howe claimed that this dipole could be considered a “sink” of sound energy. It was also observed that this phenomenon occurred at very specific wavenumbers, and results showed the dipole reducing the radiation of sound in lower Mach numbers. The TBL and the noise generated through it was a large concern, and attention was focused on the low wavenumber region of the wavenumber-frequency spectrum.

It was also Howe’s goal to understand and report on the behavior of spectral peaks caused by the influence of the TBL and its hydrodynamic properties. For example, it was detected that the turbulent shear flow influenced sound waves traveling in the streamwise direction, i.e., parallel to the wall. It could also be observed that the wall shear stress was dependent on the structure of the turbulence, leading to the generation of an unsteady BL when maintaining a no-slip condition. An experiment was conducted at subsonic Mach numbers where the boundary layer vicinity was free of sound convected by the mean flow, with no mean pressure gradient. In the analysis where a vortex sheet was used to model the effects of mean

shear, it was observed that the peak in the wavenumber shifts as a result of the presence of the vortex sheet. This was an important observation because in boundary layers with much larger wavelengths compared to widths, acoustic propagation due to mean shear effects could be safely ignored.

In 2004, Goody [9], presented an empirical spectral model of surface pressure fluctuations, where seven research groups provided experimental data for correlation. Goody describes the model as “a simple function of the ratio of the timescales of the outer to inner BL.” The timescale ratio also took into account the Reynolds number and its effects, and compared favorably to the available experimental data. Goody then began to present the concept of BL scaling, which is based on self-similarity, where variables are non-dimensionalized to be expressed as universal functions of independent variables. This allowed the parameter(s) to stay constant through a multitude of conditions.

It was Goody’s opinion that the analysis of turbulent BL conditions using self-similarity is a more challenging prospect. To scale the BL conditions, a model comprising two layers, namely the inner and outer boundary layers, was employed. The layers had their own individual scales for length, velocity, and pressure. It was noted that when considering the effects of the Reynolds number, the relationship of the layers was directly proportional to the time scale ratio employed. This two-layer model was also used to collapse the pressure spectrum into very specific frequency ranges. When using the inner-layer scales to normalize the pressure spectrum, good collapsing was observed in the higher frequencies. The higher frequencies also had a greater degree of conformity among researchers on pressure and time scales. The same could not be said about the lower and middle ranges for frequencies. The basis of the empirical model developed had its roots in a comprehensive model produced by Howe [10], in conjunction with

Chase [11]. The advantage of this model was that even with limited choices for degrees of freedom, it discerned features of the frequency spectrum of unsteady pressure (mean zero) due to turbulence.

This empirical model offered greater scaling capabilities than a polynomial curve fit; it was closer to the observed phenomenon but far less complex than other models of a similar nature. The experimental data derived through this model was comprised of 2-D, zero-pressure gradient flows. Data acquired from other models produced by other researchers was scaled and trimmed for better comparison. Background noise, generally facility related, had been known to compromise the quality of measured low-frequency data. To counteract the deficiency, data was processed with noise-cancellation techniques or obtained in an acoustically quiet wind tunnel. This ensured correct measurement of the pressure spectrum (p spectrum). On the other side of the spectrum, attenuation was observed at high frequencies. This phenomenon was attributed to the pressure transducer.

Since then, other researchers have done a tremendous amount of work on how to minimize attenuation by correctly sizing the sensing diameter on the transducer. Goody and Simpson [12] conducted other experiments on the sensor area of transducers. A pinhole was employed to reduce the effective sensing area of the transducer, causing it to work like a Helmholtz resonator. This caused the frequency response function to become a second-order function and the p spectrum near the Helmholtz resonant frequency to be amplified. In a way, this helped compensate for the attenuation observed. When Goody and Simpson used the dynamic pressure at the boundary layer to collapse the p spectra, only the very low frequencies complied. Hence, shear stress was used as the pressure scale, and a Reynolds number-

independent time scale was employed to collapse the p spectrum into a universal curve. This allowed for the encompassing of a larger band of frequencies.

Similarly, at higher frequencies using a different Reynolds number-independent time scale but the same pressure scale, collapsing of the p spectrum to a universal curve was observed. It was also noted that only the overlap range changed in the p spectrum upon modification of the Reynolds number and that the observed change was directly proportional to the Reynolds number. It was later corrected that the time scale ratio, not the Reynolds number, was the source of overlapping in the frequency range. Goody and Simpson also showed the relation between the two, i.e., the time scale ratio and the Reynolds number, and how they were directly proportional to each other. Hence, subsequent modifications to the model included the time scale ratio and allowed for greater accuracy when extrapolating to 2-D high Reynolds number flows. This scaling was unfortunately not able to deal with turbulent flows. Validity was compromised when observing flows with large turbulence intensities or large pressure gradients in the boundary layer. In flows with strictly 2-D quasi-zero pressure gradients, the pressure spectrum could be correctly predicted by the model.

Along with experimental efforts, several investigations employing numerical schemes have been performed. In 2009, Dietiker and Hoffmann [13] used DES to predict wall-pressure fluctuation. They conducted their numerical simulation using the CFD code Cobalt [14] over a backward-facing step, and they employed Menter's Shear Stress Transport (SST) as the turbulence model. This model used two equations, namely k - ϵ and k - ω , and combined the best of both. The k - ϵ equation is more advantageous in inner regions of the boundary layer, while k - ω has the upper hand in outer regions of the boundary layer; the SST switched back and forth between the two equations depending on regions in which they were more effective. The

objective of the simulation was to predict flow features such as velocity and pressure and to compare them with existing experimental data.

Dietiker and Hoffmann began by justifying the reason for using DES in their simulations. It was universally agreed that Direct Numerical Simulation (DNS) was computationally very expensive, and pure LES shared a similar problem. The advantages of DES stood out in this situation because DES allowed for RANS as well as LES to be used depending on flow location. RANS is used to solve regions near the wall, while LES is used in outer regions as well as regions of separation. Dietiker and Hoffmann, using a simple algebraic model, were able to dramatically decrease their computational time without making any compromises to the quality of the solution. In the given simulation, the turbulence model also served as a Subgrid Scale (SGS) model and was used to represent small-scale eddies, while LES was used to directly solve larger eddies. The SGS model also served as a RANS model in certain regions.

A recirculation zone was formed due to the flow detaching at the corner of the backstep, and a shear layer and corner eddy were also formed. Another time-dependent occurrence observed was the point of reattachment, as well as recirculation sizes. This DES used Menter's SST as the SGS model. Incoming velocity and turbulent kinetic energy profiles at the inlet were designed to match that of experimental work in the same vein. Since visualizing the boundary layer, capturing the recirculation and reattachment zones were a prime concern, so additional clustering was implemented on the upper and lower walls to achieve good results. After performing the simulation, it was realized that the time-averaging in the Reynolds-averaged model could not provide pressure-fluctuation data. Hence, they only presented DES results.

Other results included wall pressure, which was non-dimensionalized to coefficients for better comparison. As expected, the pressure gradient was higher on the lower surface and

highest near the reattachment point. Step-side skin-friction coefficients, mean velocity profiles in the separation and reattachment regions, as well as turbulent kinetic energy (TKE) profiles, derived through an additional transport equation, were computed and found to be in good agreement with the available experimental data. The small eddy was smaller than one step size; the recirculation zone and velocity profile were also shown to be well predicted. There was a slight underestimation of the maximum values of the TKE computed by the code when considered within this region, while a slight overestimation was observed in the shear layer downstream of the step. This behavior waned as the TKE was computed further downstream.

It was important to achieve accurate results in order to correctly derive the velocity fluctuations and, hence, pressure fluctuations. The employment of DES as compared to RANS to meet this objective was justified by the accuracy (and availability) of this important data. Surface pressure data immediately after the recirculation zone was also computed and was slightly underpredicted. On the other hand, the non-dimensional frequency at which the majority of energy resides was well predicted. Another interesting phenomenon was observed: through simulations, power spectral density (PSD) was observed to be a function of Mach number, as compared to an alternate theory that stated the independence of PSD in relation to the Mach number. Finally, the relationship between step size and frequency was derived. It was also observed that the grid density had a negligible effect on the results.

Another good example of the applications of DES to simulate wall-pressure fluctuations is in the work of Mahmoudnejad and Hoffmann [15], where results from Goody's [9] pressure spectrum model were compared to two simulation cases, as well as with their respective analytic solutions. Mahmoudnejad and Hoffmann took the time to recognize some of the work performed in recent years in the field of simulation work. The work of Lee et al. [16] was of particular

interest, due to the research conducted with a backward-facing step as well as other aspects of the flow regime such as the influence of the free-stream Mach number on the configurations.

Simulations were performed with Cobalt using a DES code and a Spalart-Allmaras (SA) turbulence model as previously described. The advantages of DES were captured using LES for turbulent regions and RANS for near-wall conditions, and the acquired results were analyzed using a MATLAB routine. The results provided power spectral density, which can be defined as the frequency response of a random/periodic signal.

As previously mentioned, two different cases were modeled—a flat plate and a duct. In the first case, atmospheric conditions for a transonic flow were assumed. Heavy clustering was implemented on the walls, and a very small time step was employed. Eleven sensors were placed along the streamwise direction to obtain sufficient flow data; pressure fluctuations were also recorded using these sensors. The first 10,000 time steps were ignored in order to achieve good mean-flow properties by eradicating the effects of initial-flow conditions.

In the second case, a subsonic flow was passed through a duct, with lower pressure at the inlet compared to the outlet and no angle of incidence introduced into the flow. Again, clustering was implemented at the walls, and sensors were placed along the upper surface of the duct as well as along the centerline. Analogous to the first case, the first 50,000 time steps were rejected in order to negate the influence of initial conditions. Results derived from the two test cases relate well with the Goody model.

1.2 Jet Flow

The second topic of discussion in this thesis is jet flow. It is important to understand the characteristics of jet flows, whether subsonic or supersonic, due to the presence of the hatch in the flow as well as the opening. The presence of the hatch can be observed in real-world

applications for vector calibration, such as thrust vectors in jet engines and rocket/missile systems. Understanding how the flow will interact with these two elements is an important objective in this thesis.

In 2005, Bogey and Bailly [17] experimented with inflow conditions to observe and understand corresponding effects on flow, its development, and, consequently, the effects of flow on the local sound field using LES simulations. They did so using a circular jet at Mach 0.9 and Re at 4×10^5 . Using numerical schemes from one of their previous works [18] that used low dispersion and dissipation properties, Bogey and Bailly solved the Navier-Stokes equations. Spatial discretization was solved using a 13-point finite difference scheme, while integration was solved with an explicit six-stage Runge-Kutta algorithm and applying additional filtering in order to ensure numerical stability. They also claimed that the resolved scales were left unaffected by the subgrid energy-dissipating scales, which helped preserve the Re of the jet. In their opinion, the preservation of Re would not have been possible with eddy-viscosity models. A dynamic Smagorinsky model was used to artificially decrease the flow Re , while a sponge zone [19] at the outflow was used in conjunction with the non-reflective boundary condition (BC) to compute the noise generated.

Bogey and Bailly computed the flow up to an axial distance of 20 times the value of the jet radius; a radial distance of 15 times the jet radius was used for computing the sound field. The radius of the jet also dictated the velocity profile, which was perceived to be a hyperbolic-tangent. A Crocco-Buseman relation was used to describe the density profile. Shear-layer velocity profiles were disturbed in order to initiate the turbulence transition; this was done to keep the spurious acoustic waves to a minimum and also free of divergence. Jet azimuthal mode combinations were used to dictate forcing on the inflow where velocities, both radial as well as

axial, were modified at every time step. After initialization of the simulation, Bogey and Bailly noted that the “LES mode” simulation, where the first four azimuthal modes were removed, developed its jet flow slower than that of the “LES shear” simulation, where the shear layer was 40% less than that of its counterpart. The latter showed an increase in turbulence intensity, along with quicker transition to turbulent flow.

On the other hand, this simulation slowed down the development of the jet flow, and past the potential core, a decrease in the aforementioned turbulence intensities was also observed and led to a decrease in noise generated in the axial, i.e., downstream direction. This came at a cost of increased noise in the radial direction. The most important development acquired from the experiment was an understanding of the effects of removing the first four azimuthal modes. It was observed that this change caused a decrease in turbulence intensities and, consequently, noise. It also notably slowed the growth of the jet.

Bogey and Bailly recommended continuing this work in order to decrease sideline pressure levels, because an over prediction was observed in the current scheme. It was suggested that the source of error may be the shear layer or, more precisely, its high radial velocity perturbation intensity. This was also directly responsible for the higher sideline noise amplitudes, which could be seen by the correspondence in the peaks and hence could be associated with the development of shear-layer turbulence.

In 2006, Tinney et al. [20], in conjunction with the Laboratoire d’Etudes Aérodynamiques of France and Syracuse University in New York, discussed the achievements made in the field of turbulence modeling of high-speed jet flows, in order to understand sound sources and their mechanisms. They began by reiterating the fact that even the latest experimental devices contributed to flow interference; acoustic sources, as well as turbulence

dynamics were still difficult to model due to the lack of accuracy brought on by the presence of said devices. Instead, efforts were being made to better understand the near-field pressure region. They determined that flow characteristics observed in this region could be mapped to the turbulent large-scale events detected in the flow, and in turn, the turbulent large-scale events could be mapped to the sound generated in the acoustic field.

The objective of Tinney et al. was to discuss the process and results of using a Spectral Linear Stochastic Estimation (SLSE) to observe the shear layer in a jet in order to dynamically estimate the flow field. This technique was used to filter out data pertaining to the turbulence structure. This provided flexibility to better understand the components behind the generation of noise itself. The first SLSE-based experiment was published in 1997 and was shown to have good results for single time estimates. The changes made to this technique allowed it to preserve a conditional event's spectral characteristics when a divergence was observed in the conditional and unconditional parameter's spectral densities. Doing so allowed for accurate acquisition of data from the pressure signatures and a continued estimation of dynamic conditional velocity in the potential core as well as the mixing layer. Also, the application of the estimation procedure allowed for greater accuracy when approximating the velocity field in a low-order model, especially for accurate source-term models.

This experiment, conducted in the anechoic chamber at Syracuse University, utilized an axisymmetric jet at Mach 0.6 and Re of 6.4×10^5 at 298K. In order to accurately accrue experimental data, 15 pressure transducers and a Laser Doppler Anemometer (LDA) were employed. The LDA used a backward scattering technique with a 3W argon-ion laser, and both pressure and velocity were measured at a sampling rate of 30k Hz to 40k Hz. It is important to note that the setup only gathered streamwise velocity data. The radial positions for the

transducers and the LDA were chosen in order to have pressure velocity cross spectra at critical regions, including at the center of the potential core. This was done to improve the spatial resolution of the dynamic model via interpolation using cubic spline and a back-substitution algorithm. The data was then resampled and run through a filter to arrive at the final cross-correlation matrix with data that covered the entire near-field region.

Tinney et al. proceeded to decompose the model using Lumley's [21] Proper Orthogonal Decomposition and then recreated it in order to calculate the acoustic source field for further analysis using eigenfunctions acquired from the decomposition. This led to a sectional volume reconstruction to acquire source-field results. Features observed near the jet nozzle, including the high frequency, were shown to increase in the axial direction and were stimulated by the minutest of dimensional events. The acquired results served two major purposes: first, a more accurate approximation of the Lighthill source term, and second, a comparison with Particle Image Velocimetry (PIV) data previously acquired. The results also helped broaden comprehension of the relationship between the source field and the velocity field, as well as understand that the production of sound energy from the flow generated turbulent kinetic energy. Tinney et al. hope to further their work by performing similar experiments on flows with radiating source structures.

In 2007, Yan et al. [22] investigated subsonic jet flows with smooth- and serrated-lipped nozzles, and showed great interest in the previous work covering the importance of nozzle modeling and its effect on the Overall Sound Pressure Level (OASPL). They also showed great interest in the work of Bodnoy et al. [23] related to the importance of researching the effects of including nozzle model geometry in numerical simulations and its impact on forcing parameters, especially pertaining to jet turbulence and sound field. The work of Bodnoy et al. also showed

that the inclusion of the model removes the dependence of the characteristics on the forcing functions.

Yan et al. then proceeded to discuss the optimum computational scheme that could be applied to the problem. Even though there were many RANS schemes from which to choose, RANS itself still had trouble with flow features that affect sound propagation, such as low frequencies generated by large-scale motions. LES could perform this task well but came at a cost of computational power due to requiring a higher density grid, even near the wall. Hence, DES was selected, using the best of both worlds, and was combined with Ffowcs-Williams and Hawkings [24] aeroacoustic analogy for farfield Sound Pressure Level (SPL) calculations, as well as Wilcox's $k-\omega$ turbulence model for turbulent dynamic viscosity. Their end goal was to analyze the application of DES schemes and validate it for use in the calculation of jet noise.

The next question to be addressed was that of the DES-generated "grey area" problem, i.e., the region between the RANS boundary layer and that of the fully developed LES. To be more precise, the technique used to switch between RANS and LES in a model had not been perfected, and this could hinder the proper computation of the LES zone by ineffectively convecting eddy viscosities. In order to mitigate this problem, Yan et al. [25], in their previous work, came up with a filter that was applied to the length scale. Its application showed a great impact on the ability to mitigate the onset of turbulence by stretching shear-layer grid cells. They also took time to contemplate an alternate strategy, Implicit LES, i.e., removing the need for subgrid modeling. The model generated was then exposed to non-reflective boundary conditions as well as two damping zones—one in the nozzle inlet and the other in the outlet.

Once the computational scheme, turbulence model, boundary conditions, and special modifications, namely reflective BCs and damping algorithms, were selected, Yan et al.

determined the numerical aspects of the experiment. A finite volume scheme was employed to discretize the Navier-Stokes Equation (NSE) applied to a domain 50 diameters deep in the axial direction and 18 diameters wide in the radial direction. Using a structured grid, 3.8 million cells were used to resolve the basic profile, and 11 million cells were used for the serrated-edge profile. Clustering was performed in near-wall regions as well as at the shear layers. Nozzle lips and the cone tip were also densely clustered for obvious reasons, and a $Y^+ < 2$ was maintained at all walls. The inlet BC was dictated by the two flow Mach numbers, and the turbulence intensity was set at 10%. Finally, the outflow velocity was set at 10 m/s. With these BCs, the unsteady simulation used a converged RANS solution as a starting condition. The LES section used a blending function that incorporated a Central Differencing Scheme (CDS) and Total Variation Diminishing (TVD) upwind-based scheme. This function forced the TVD scheme at the near-wall regions and the CDS at the far regions. The computation Δt was set at 2.5×10^{-6} s.

Their first computation showed a comparison of their DES code versus the original, which validated the modification. Improvement was seen in the nozzle exit-flow structure, and greater accuracy in the frequency prediction was also observed. Pressure was underpredicted in the region, causing an over prediction of axial velocities. Apart from the near-jet axis region, satisfactory velocity profiles were observed along the axial direction. Upon assessing turbulent structures, it was found that low mixing took place in the shear layer observed between the bypass streams and the core. This observation was attributed to the shear layer being thin and stable, and was shown to be consistent with other findings. The serrations were shown to enhance mixing by causing an earlier transition to turbulence. This also led to the formation of a greater number of smaller eddies and a finer structure near the serrated lip. Results of the OASPL were also found to be in agreement with similar data acquired by research conducted in

the United Kingdom, observing a deviation of no more than 3 dB. It was also found that the grid density was not as pertinent to the farfield as to the near field. Conclusions also pointed to the fact that the inclusion of the serrations on the lip reduced the overall noise generated by approximately 2 dB. Again, good agreement was found between numerical and experimental data.

In the same year, Elzawawy et al. [26], using Stereo Particle Image Velocimetry (SPIV), conducted experiments on subsonic jets at Mach numbers 0.3, 0.6, and 0.9 in three different gases in order to better understand the effects of flow properties such as density on turbulence. It was well known that the growth of free shear flow is reduced by compressibility, and to no small degree. More than 30 years' worth of research had gone into this problem, and numerous researchers, including Papamoschou and Roshko [27], had spent time and effort into characterizing shear-layer compressibility via the convective Mach number. Different studies have also shown that with the increase of compressibility effects, growth of the mixing layer is diminished, verified by DNS and LES experiments. The objective of Elzawawy et al. was to further the work of Wang [28] via emphasis on flow-field turbulence measurements.

Due to the requirements of the experiment, Elzawawy et al. had to design a facility that had the desired properties when creating a jet flow. In lieu of a plenum chamber, a simple steel tube was chosen in order to have a fully turbulent flow from the beginning. The concern of instabilities in the flow was also dealt with by taking the aforementioned step, as well as allowing for jet/shock-related experiments. The setup included a pressure regulator that supplied a constant amount of pressure from the gas tank, which in turn led to a more stable jet Mach number. To ensure that the Mach number was accurate, a pressure gage was placed close to the pipe exit to maximize certainty and allow for quick changes to pressure. It was found that using a

set of one-dimensional adiabatic frictional-flow equations for iterating the Mach number was more than satisfactory, and its results compared well to data derived from the flow-visualization process.

Velocity was measured using 3D PIV using two solid-state lasers mounted on a laser arm, which allowed for a variable light-sheet source. This was done in conjunction with two cameras stationed perpendicular to the flow, at an angle of 40 degrees, to correctly capture all three components of velocity. Appropriate modifications were made in order to compensate for the angles and other camera-related issues, especially the amount of light captured. Due to the ease of acquisition and its non-toxic properties, olive oil was chosen as the tracer compound, and by using atomizers stationed inside the piping system, fine droplets were produced. Ambient flow seeding was also performed via a nozzle placed externally to the jet pipe. In order to capture sufficient data, the laser was pulsed between 0.5 μs and 10 μs , depending on the speed of the jet.

When computing the data derived from the experiment, it was realized that the helium jet had the highest spreading rate, followed by nitrogen, and krypton with the lowest spreading rate. Results also showed that helium had a much higher exit velocity when compared to nitrogen, and with increasing Mach number, it took the flow a longer distance to decelerate. Longitudinal velocity fluctuations, and consequently turbulence, were also shown to be directly proportional to the Mach number. It was noticed that the helium jet had more turbulent fluctuations when compared to the nitrogen jet, leading to the conclusion that the fluctuations were also directly proportional to the spreading rate; this also commented on the state of mixing when considering density as a propagating factor. As expected, the jet exit, i.e., near-field-generated shear layers, produced the greatest amount of shear observed in the flow and were found to be highest in the

helium jet. Centerline velocity data was compared to that generated by Wang [28], and the trends found between the two studies were observed to be in agreement.

Recently in 2009, Liu et al. [29] studied the acoustic effects of jet flows using LES techniques. Their objective was to observe the effects of a jet flow at Mach 1.5 under different Nozzle Pressure Ratios (NPRs) using a convergent-divergent nozzle to gain further knowledge of near-field properties and flow structures. Varying the NPR allowed them to observe the shock cells interact with the exhaust under different conditions, and also allowed for analysis of the effects on the noise generated. From the highly experimental work of Tam [30], Liu et al. stated that at approaching high Reynolds numbers, supersonic jet flows generated noise by the presence of wave instabilities as well as turbulent flow structures. Other work [31] also showed that noises produced by downstream shocks are the predominant sources of shock noise in similar cases.

The work conducted by Liu et al. was performed in collaboration with the University of Cincinnati (UC); Liu et al. were responsible for the numerical component, UC for the experimental section, and the Naval Research Laboratory for the numerical simulations. In the companion paper [32], simulations of the computational methodology developed in the paper are discussed, and using LES, pressure ratios for over- and under-expanded nozzles are computed and compared to acquired experimental data. This paper also makes an effort to emphasize acoustic properties and near-field flow region predictions.

Due to the way in which the nozzle throat contraction is designed, there were no conditions under which a flow existed without a shock. Hence, the nozzle in the given experiment was designed such that the NPR needed to be set at 3.7 in order to have the exit pressure equal the ambient pressure, and a range of 2.5 to 5.0 was simulated. In each case, the

data was collected only after a fully developed flow was generated. It was observed that in the case with a NPR of 4.0, the probe density had to be doubled to 0.1D from 0.2D.

Results showed that when acquiring static pressure, no screech tones were observed in the case where NPR was set at 2.5 and pressure iso-surfaces were toroidal in shape. It was also shown that iso-surfaces of the other cases depicting these tones had a clockwise motion and propagated downstream, similar to a helix, and that these tones were easier to discern in over-expanded nozzle cases.

Liu et al. deemed that three discreet regions were required to properly account for the noise generated in the flow. The first was the near-stream region, i.e., immediately downstream from the lip of the jet. Here, large-scale motions generated by the nozzle lip interacted with the shock cells. The second region was defined by the amplified interactions of the motions and shock cells further downstream, which were shown to be the primary contributor of noise in the system. The third region was attributed to the fact that flow mixing was observed and was also a great source of noise generation.

CHAPTER 2
MODEL DESCRIPTION

2.1 Generic Geometry

The geometry of the jet for the current investigation revolves around the central jet exhaust. The overall dimensions of the exhaust pipe were set at 20 inches in length and 6 inches in diameter, as shown in Figure 1 and Figure 2.

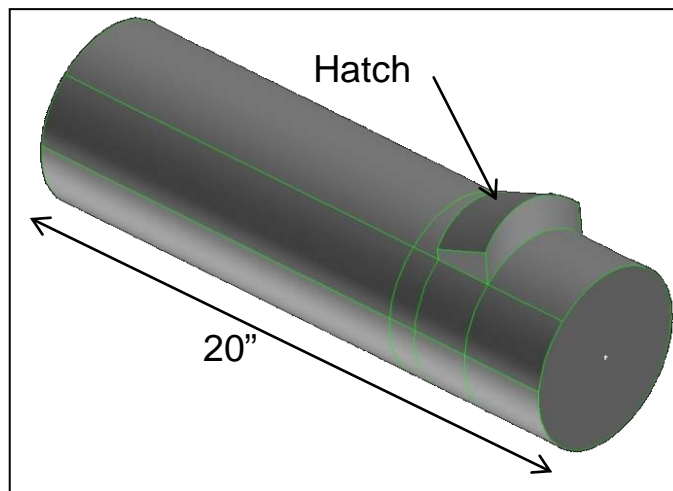


Figure 1. Isometric view of jet pipe

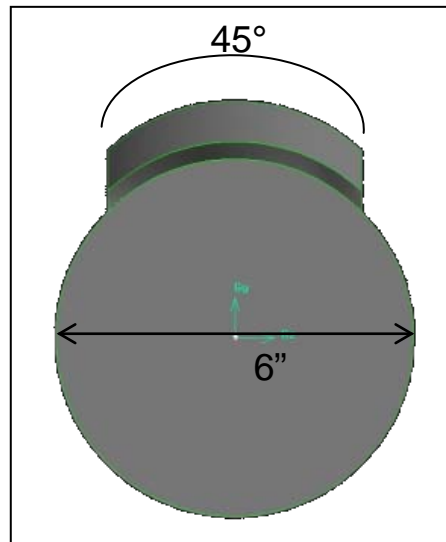


Figure 2. Front view of jet pipe

An opening of 2 inches in length and an arc angle of 45° were set on the surface of the pipe, 15 inches from the inlet. Figure 3 further illustrates the position of the opening as well as the “hatch surface,” which is identical to the dimensions of the opening. It is angled at 20° using a point of rotation 1 inch behind the opening. This is selected in order to simulate a hinge mechanism that would be employed in controlling the hatch position, varying it as required.

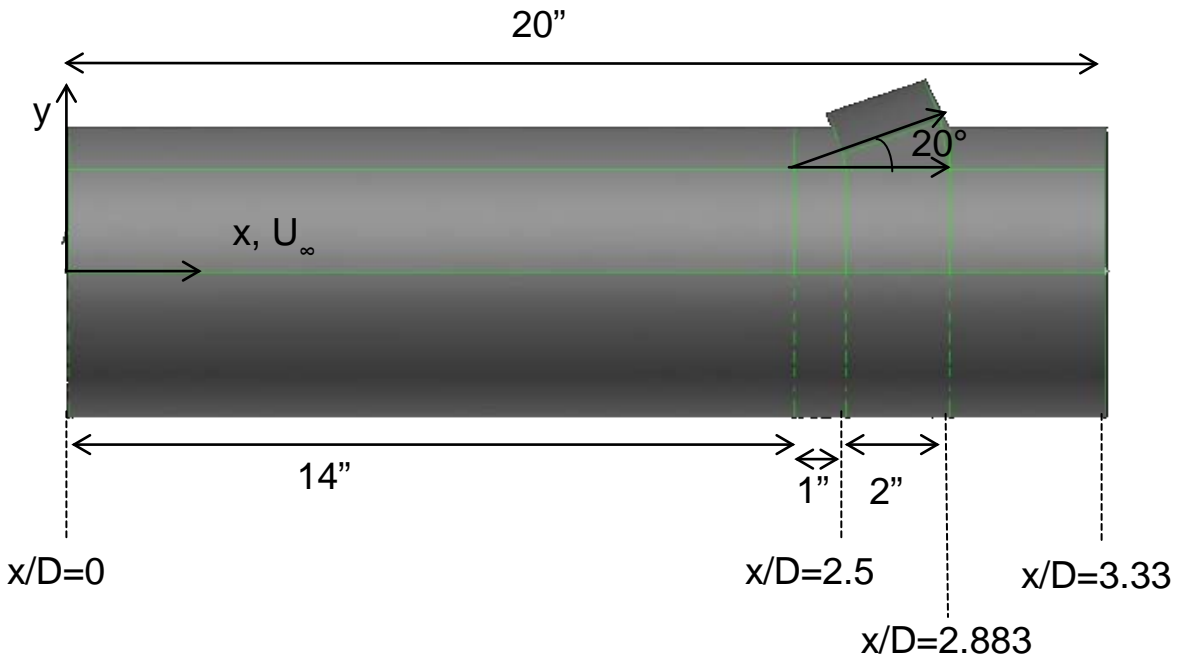


Figure 3. Opening and hatch with respect to jet exhaust pipe

Due to the complexity of the hatch, a few simplifications were employed. The wall thickness of the exhaust pipe was assumed to be infinitely thin. And, from this assumption, the hatch was assumed to be “floating in place” without any physical connectors such as hinges and legs attaching it to the pipe itself.

2.2 Determining Domain of Solution and Boundary Conditions

Through the course of the project, changes were made to the domain of solution to optimize the conditions and capture the information as accurately as possible. The solution domain was a cylinder with a diameter of 30 inches. The length of the cylinder was varied to

better understand the phenomenon as observed through the various test cases. The best domain was then selected for the final version, from which most results were gathered and presented.

Similarly, the boundary conditions were varied and changed to match the changes made to the domain of solution. The first half of the project was conducted with a supersonic inlet, and the latter half with a subsonic inlet. The jet-flow pipe remained unchanged in geometry throughout the entire duration of the project.

Currently, three major revisions were made in the project by varying the solution domain, boundary conditions, mesh type and quality, and solver type. With each successive variation, the best elements of the previous cases were implemented to determine the optimum configuration.

CHAPTER 3

MODEL VALIDATION

Once the model was determined, it was imperative to ensure that validated schemes were employed in the computation of the hatch. To do this, the computational efforts of Dietiker and Hoffmann [33] were used to validate supersonic jet flow through a pipe. The aforementioned work uses the computational software COBALT to solve for both a fully expanded and underexpanded jet flow using RANS-SA, DES-SA, and DES-SST as the turbulence modeling schemes. The numerical schemes were then compared to experimental data generated by Panda and Seasholtz [34]. Using a similar methodology, the work performed for the fully expanded jet was recreated using GAMBIT [35] and executed in FLUENT [36] employing the geometry and boundary conditions designated for the test cases to be analyzed in this paper. Since the case shown by Panda and Seasholtz and Dietiker and Hoffmann did not have a hatch, it was decided that the validation case geometry would be cut off just before the hatch.

3.1 Model Geometry, Domain of Solution, and Boundary Conditions

While attempting to replicate as much of the original jet pipe geometry as possible, a few minor changes had to be made. First, the model was scaled down to one-sixth of its original size for the fully expanded validation case and cut off just before the hatch. This resulted in a jet pipe with a diameter of 1 inch and a length of $x/D = 2.5$. The changes were introduced in order to reduce computation time. Since the zone of interest in the work to be performed was around the hatch, the domain of solution was restricted to $x/D = 15$ because the region of interest did not exceed $x/D = 10$. The diameter of the domain of solution was set at $y/D = 8$.

As for boundary conditions, a pressure inlet was used to generate the supersonic flow, and the outlet was set as a pressure outlet. The remaining faces of the domain of solution were set as farfield, as shown in Figure 4.

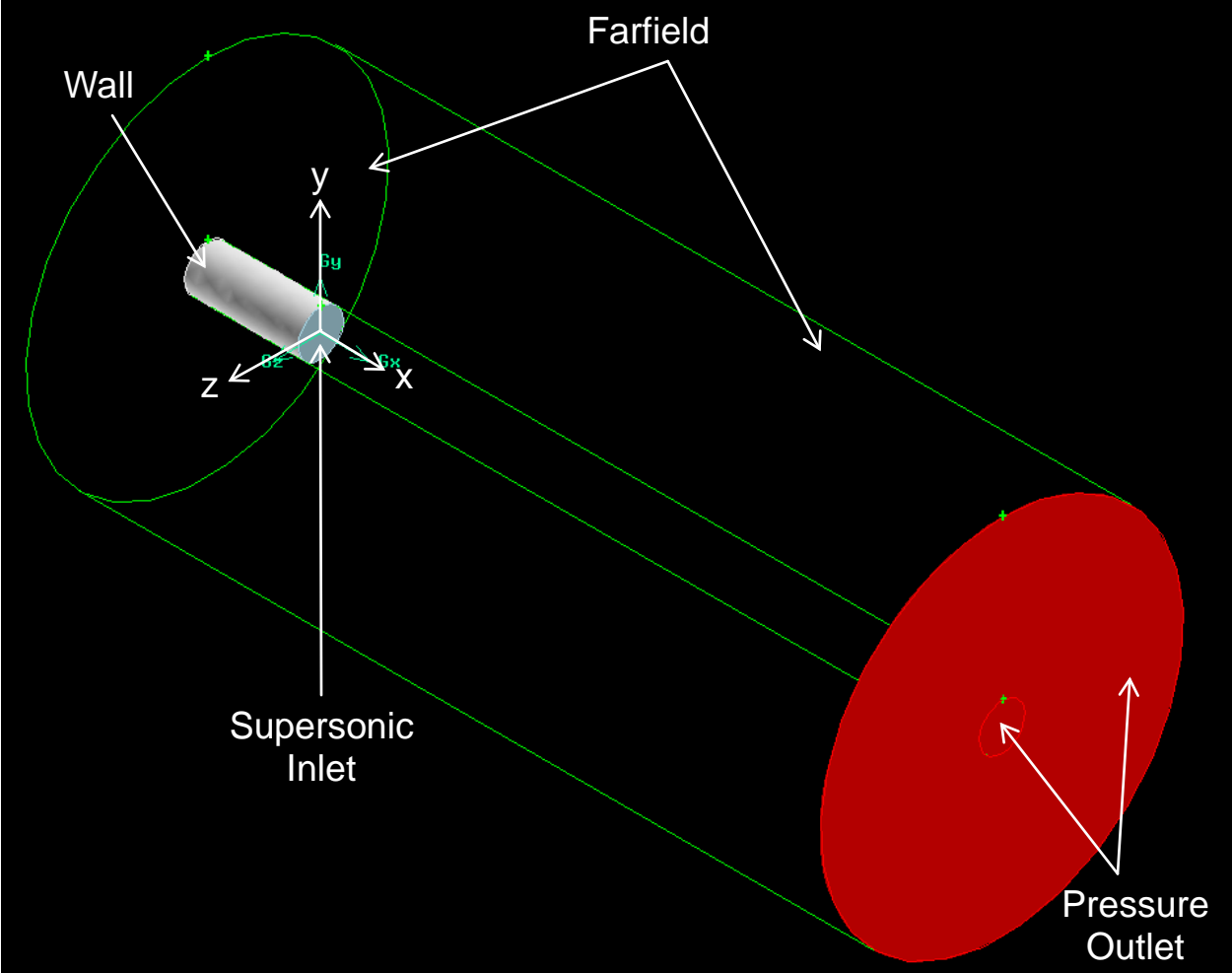


Figure 4. Validation case: Boundary layer

3.2 Meshing

A coarse unstructured grid was generated for the cases using a little more than 500,000 tetrahedral cells. The mesh had a skewness of 0.75, and only 9.7% of the cells had skewness over 0.5. As shown in Figure 5, a dense mesh was used along the centerline of the geometry to accurately capture velocity fluctuations along with other data used to compare the validation test cases to that of Dietiker and Hoffmann, as well as the experimental data of Panda and Seasholtz.

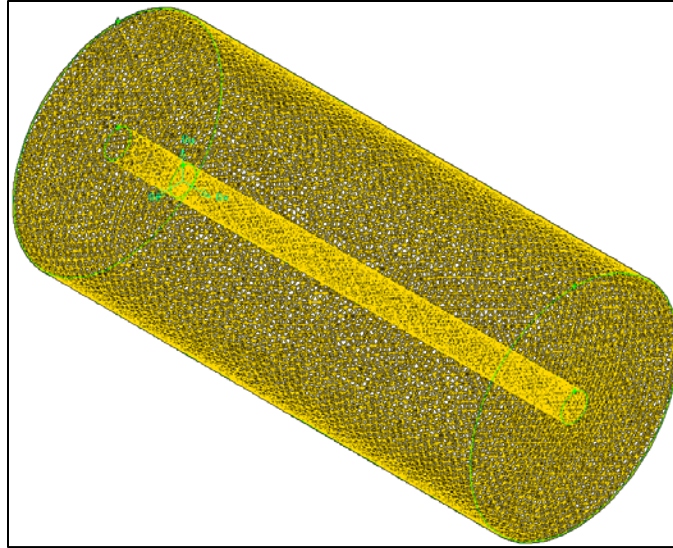


Figure 5. Validation case: Fully expanded jet mesh

3.3 Results

Results acquired after a transient analysis using FLUENT through the High Performance Computing Center (HiPeCC) at Wichita State University for the test case follow. Figure 6 shows the centerline velocity results from the fully expanded jet and are compared to the experimental data of Panda and Seasholtz. It can be noted that the data acquired is in good agreement with the work shown by Dietiker and Hoffmann as well as the experimental data generated by Panda and Seasholtz.

Figure 7 shows the velocity contour of the jet, which is also in good agreement with the velocity contours derived by Dietiker and Hoffmann.

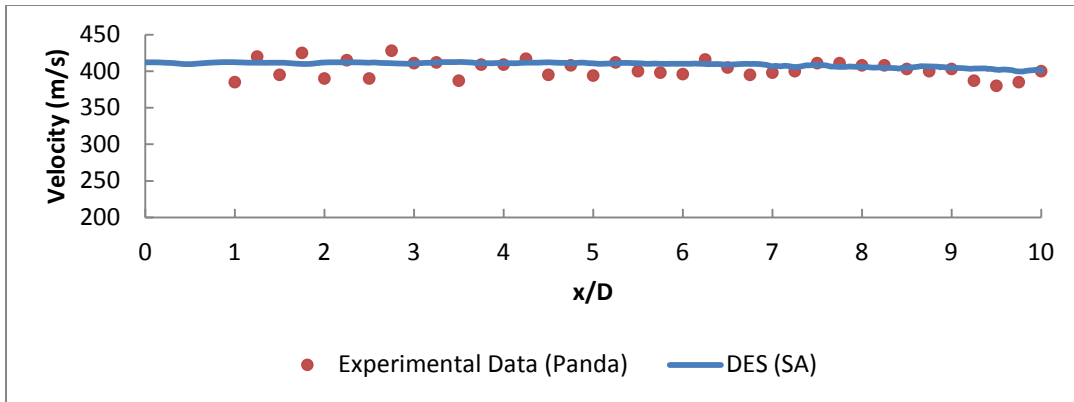


Figure 6. Validation case: Centerline velocity

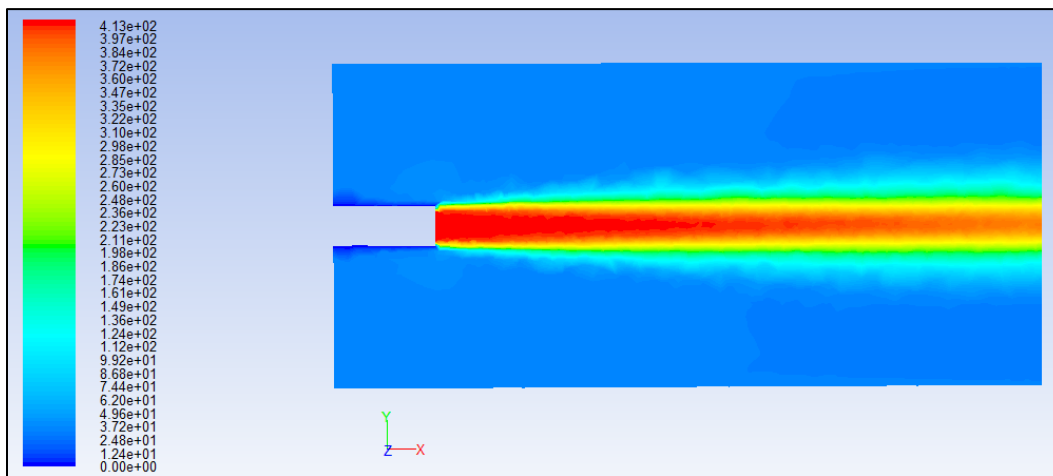


Figure 7. Validation case: Contours of velocity magnitude

Velocity profiles at various sections along the flow direction are shown in Figure 8. As can be seen, this data, too, is in good agreement with the experimental data generated by Panda and Seasholtz.

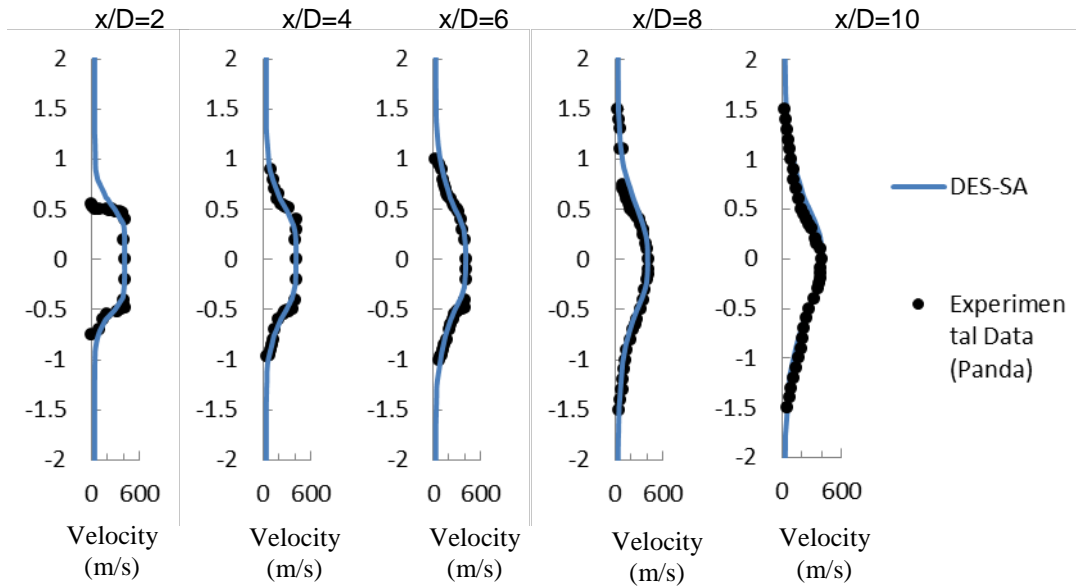


Figure 8. Validation case: Velocity profiles

CHAPTER 4

TEST CASE VERSIONS

4.1 Test Case Version 1

4.1.1 Geometry, Domain of Solution, and Boundary Conditions

After performing the validation case, the first full-sized version was initiated. The jet pipe with hatch geometry described in Chapter 2 was employed. Since the hatch was now incorporated into the geometry, a domain of solution larger than the one utilized by Dietiker and Hoffmann [33] would be optimal. Since the hatch was not at a large angle of inclination, it was decided that the diameter of the domain of solution would be set at $y/D = 5$, resulting in a full-sized domain diameter of 30 inches. Similarly, the length of the domain of solution was set at $x/D = 20$, thus a length of 120 inches. The boundary conditions for the solution domain were kept consistent with the boundary conditions used in the validation case.

4.1.2 Meshing

The new mesh with the modified length now had 538,380 cells with a max skew of 0.795, as illustrated in Figure 9.

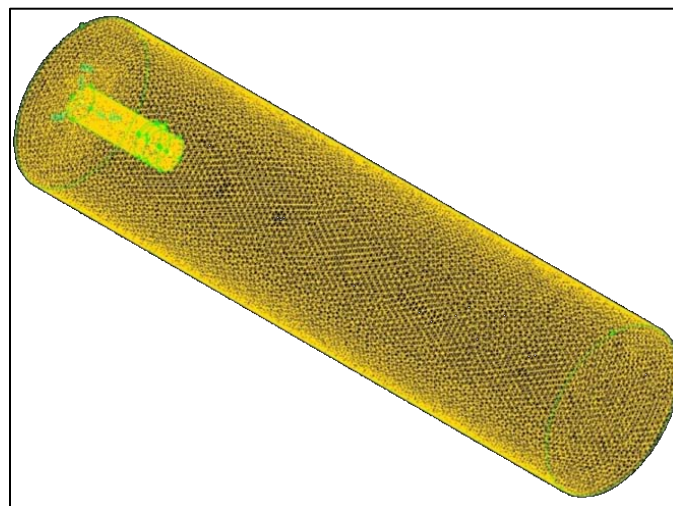


Figure 9. Version 1: Unstructured tetrahedral mesh

To realize a better understanding of the cell distribution, Table 1 and Table 2 provide a breakdown of the same, using volumes and skewness range as distinguishing criteria.

TABLE 1

VERSION 1 CELL DISTRIBUTION—VOLUME

Volume	Number of Cells in Volume
Internal Cylinder	34,065
Hatch	2,650
Domain of Solution	501,665
Total	538,380

As can be seen in Table 1, the hatch and the cylinder have good cell density.

TABLE 2

VERSION 1 CELL DISTRIBUTION—SKEWNESS RANGE

From Value	To Value	Count in Range	% of Total Count
0	0.1	40,824	7.58
0.1	0.2	89,385	16.60
0.2	0.3	138,263	25.68
0.3	0.4	138,881	25.80
0.4	0.5	77,556	14.41
0.5	0.6	38,502	7.15
0.6	0.7	13,627	2.53
0.7	0.8	1,342	0.25
Total		538,280	100.00

Again, as shown in Table 2, less than 10% of cells were skewed over 0.5, affirming the quality of the mesh.

4.1.3 Solution Procedure

Once the mesh was complete, it was exported to FLUENT, which allowed for the application of the aforementioned boundary conditions and other criteria. For this case, the Spalart-Allmaras turbulence equation was used. The transport equation for the model is

$$\frac{d}{dt} \int_V \omega \, dV + \int_V \nabla \cdot (\omega \mathbf{u}) \, dV = \int_V \nu \nabla^2 \omega \, dV + \int_V S_\omega \, dV \quad (1)$$

where ν_t is identical to the turbulent kinematic viscosity except in the near-wall (viscosity-affected) region, G_ν is the production of turbulent viscosity, Y_ν is the destruction of turbulent viscosity that occurs in the near-wall region due to wall blocking and viscous damping, C_{b2} and C_{μ} are constants, ν is molecular kinematic viscosity, and S_ν is a user-defined source term.

The solution was first converged at a steady state, and then, using a time step of 10^{-6} s, a transient solution computed until 0.1 s.

4.1.4 Results

Upon computing the simulation in a transient solution up to 0.1 s, the following results were attained. Figure 10 and Figure 11 depict the contours of static pressure and centerline pressure at 0.1 s, respectively. It can be observed from the contours of pressure that a region of low pressure develops under the hatch, while a region of high pressure develops before and after the pipe opening.

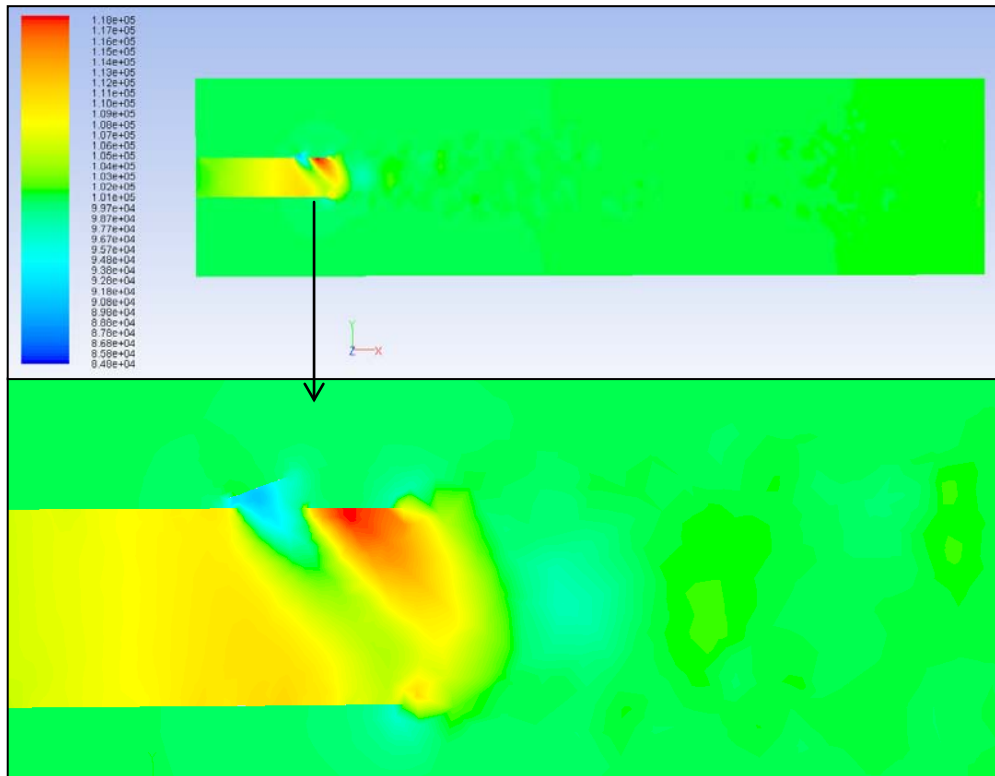


Figure 10. Version 1: Pressure contours at 0.1 s

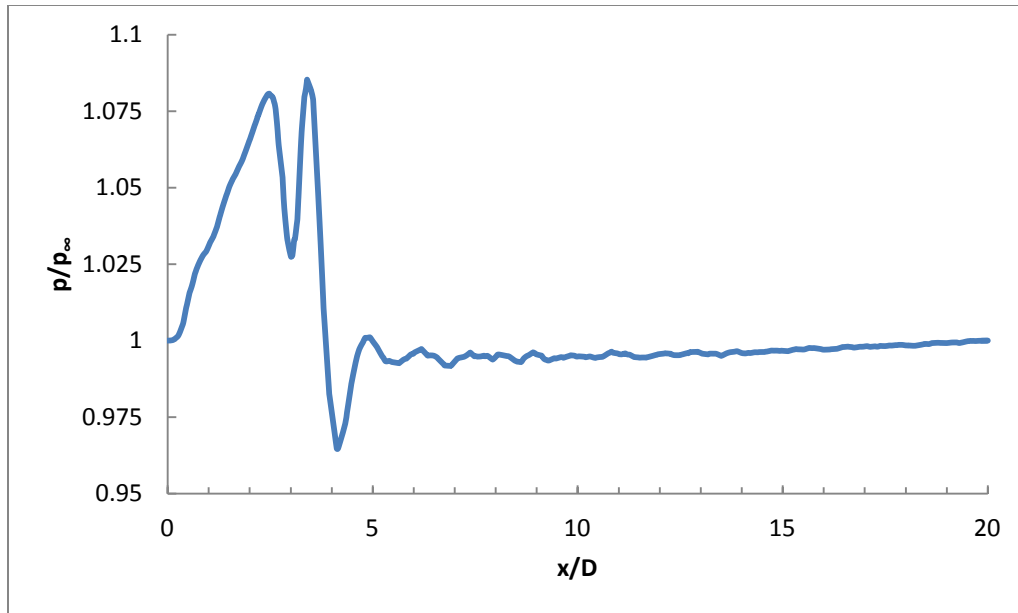


Figure 11. Version 1: Centerline pressure at 0.1 s

Analyzing the centerline pressure leads to the conclusion that a compression wave was formed because of the presence of the opening, and a second compression wave was formed outside the jet pipe. Beyond $x/D = 5$, the pressure was shown to stabilize, and at $x/D = 20$, ambient pressure was reached, thereby justifying an increase in the length of the solution domain.

As observed from the pressure data, Figure 12 and Figure 13 affirm the existence of the two compression waves, and it can be seen that the exhaust flow velocity profile was allowed to develop unhindered due to the length of the domain. In addition, allowing for $y/D = 5$ was reasonable and helped to clearly show the velocity profile in the downstream region. The centerline velocity showed the presence of a compression wave at the opening and a reflection shock outside the jet pipe, which concurs with the centerline static pressure as well, and illustrates the dramatic deceleration of the flow. This deceleration can also be observed in the RANS-SA calculation performed by Dietiker and Hoffmann, and can be attributed to under-prediction of the model in the farfield.

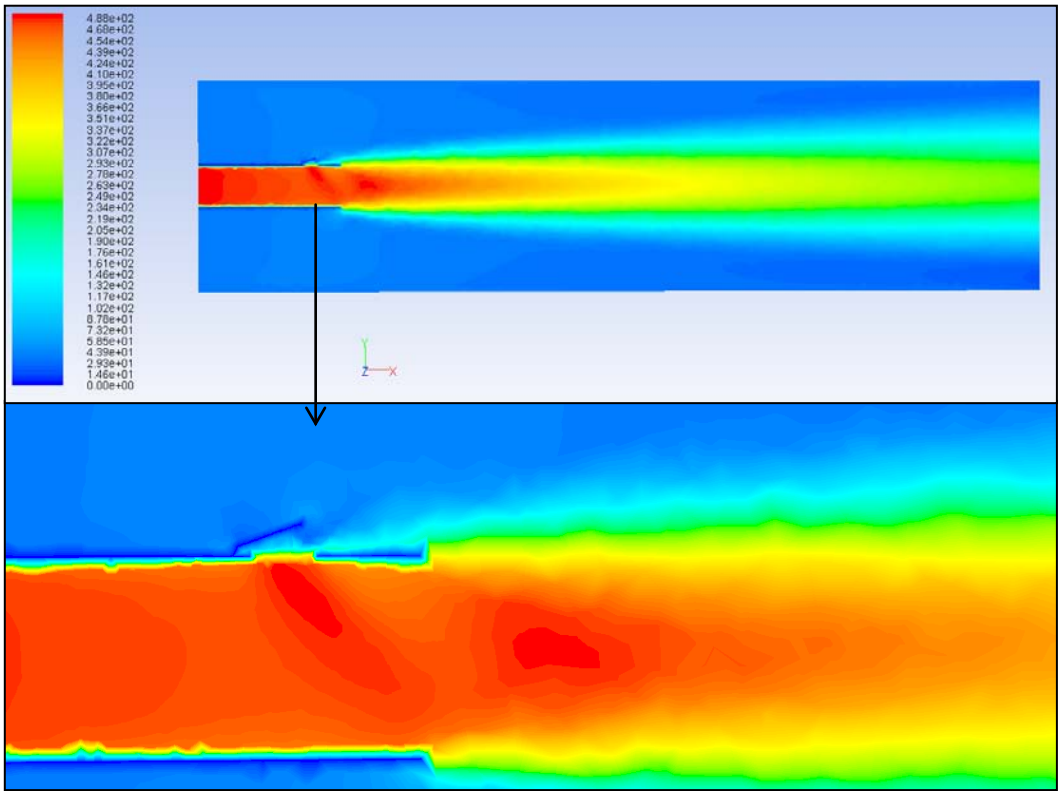


Figure 12. Version 1: Contours of velocity magnitude at 0.1 s

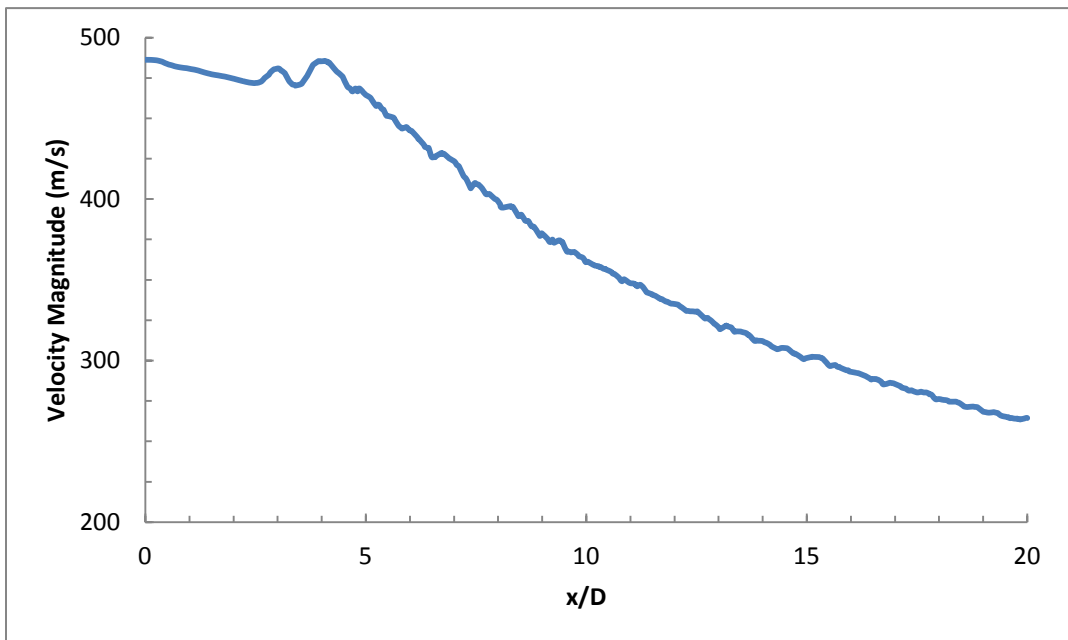


Figure 13. Version 1: Centerline velocity at 0.1 s

Since the velocity contours did not provide sufficient data pertaining to velocity under the hatch, iso-surfaces using TecPlot [37] were used to generate the same. Figure 14 clearly shows that there is a large region under the hatch that undergoes reversed flow. Figure 15 displays the x-velocity profiles at $x/D = 2.5$, 2.667 , and 2.833 , i.e., under the hatch. It can be observed from these three figures that the presence of the hatch and opening dramatically influences the flow in that region. Figure 15b shows that there is flow mingling observed between the supersonic jet and the freestream, which is in good agreement with the low pressure observed.

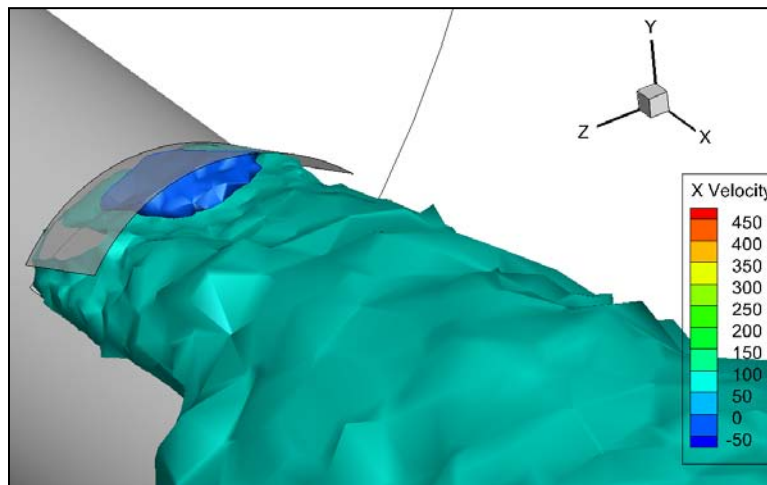


Figure 14. Version 1: X-velocity iso-surface at 0.1 s

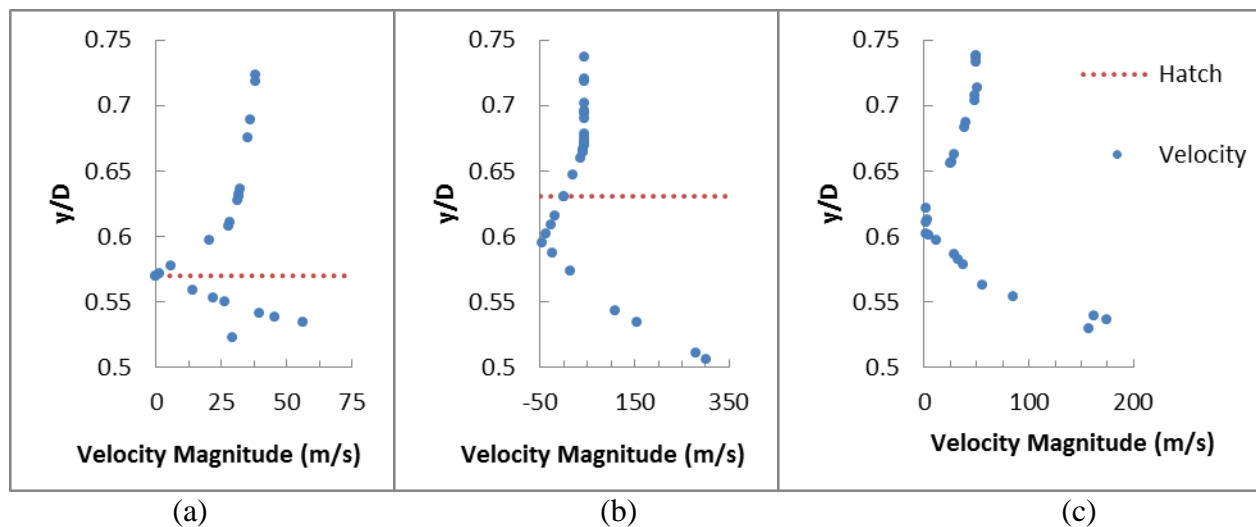


Figure 15. Version 1: X-velocity profiles at (a) $x/D = 2.5$, (b) $x/D = 2.667$, and (c) $x/D = 2.833$

Figure 16 depicts the Turbulence Viscosity Ratio (TVR) plot, which also shows good results, since the turbulence can be traced back to the opening and hatch as observed. The TVR observed at the outlet, on the other hand, is an artifact of reversed flow observed during the steady-state convergence and is not a phenomenon observed in nature. In order to counteract its effects, changes to the length of the domain of solution were implemented.

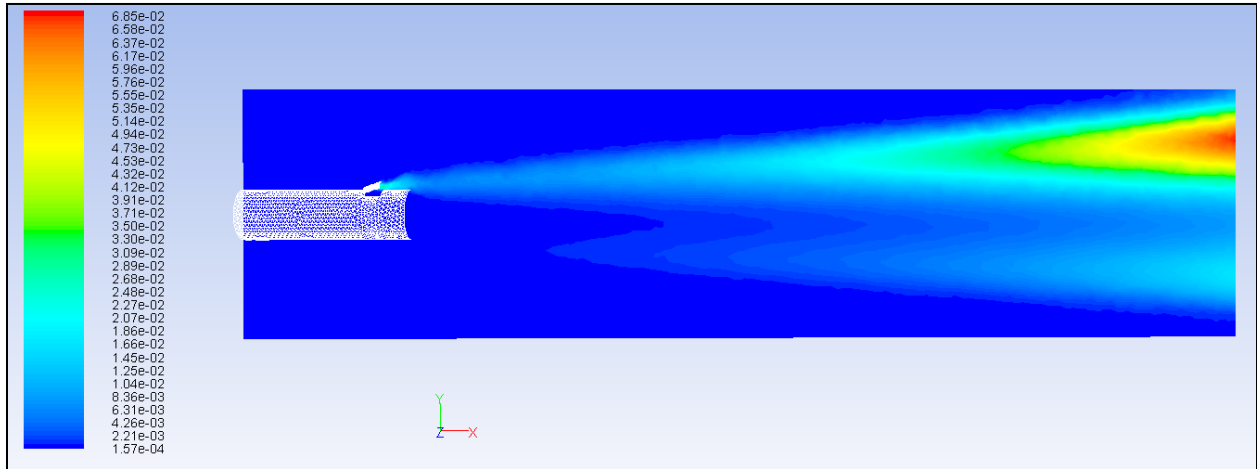


Figure 16. Version 1: TVR with mesh at 0.1 s

4.2 Test Case Version 2

4.2.1 Geometry, Domain of Solution, and Boundary Conditions

After the success observed in Version 1 with supersonic flow, it was necessary to utilize the geometry in subsonic conditions. Hence, the Mach number was reduced from 1.4 of the supersonic case to 0.5 for the new subsonic case. Due to the decrease in velocity, and now knowing the impact it would have on pressure and velocity fluctuations, it was decided that the new length for the domain of solution would be 180 inches, i.e., $x/D = 30$.

Every other boundary condition was maintained from Version 1. It was also decided that the LES scheme would be employed in this version to accurately capture the fluctuations of pressure, especially around the hatch. Doing so allowed for accurate pressure-data acquisition, which in turn allowed for SPL data generation.

4.2.2 Meshing

Since the LES scheme was employed, a clustering region around the hatch and opening was created. The region around the hatch where a greater density of cells was provided is shown in Figure 17.

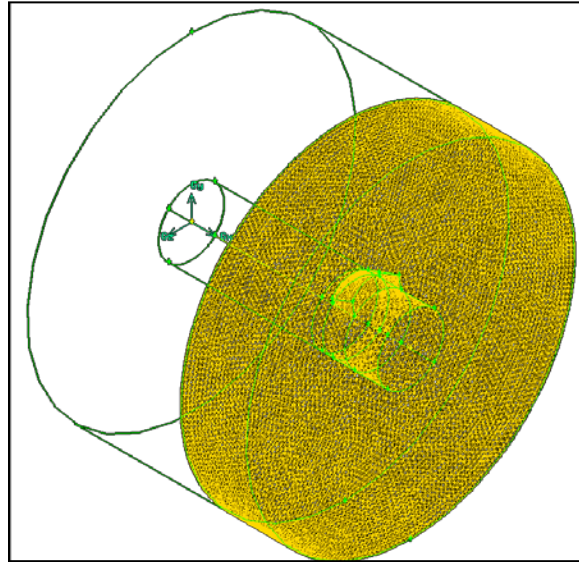


Figure 17. Version 2: Unstructured mesh around hatch and opening

To illustrate a better understanding of the cell distribution, Table 3 and Table 4 provide a breakdown of the same, using volumes and skewness range as distinguishing criteria.

TABLE 3

VERSION 2 CELL DISTRIBUTION—VOLUME

Volume	Number of Cells in Volume
Internal Cylinder	23,389
Hatch	5,155
Region around Hatch	202,899
Rest of Domain of Solution	1,379,601
Total	1,611,044

With the addition of a clustering region around the hatch, more accurate predictions for velocity, pressure and turbulence fluctuations were expected. Cell density within the hatch

volume was also increased in order to accommodate greater accuracy. Overall cell density of the domain was also increased.

TABLE 4
VERSION 2 CELL DISTRIBUTION—SKEWNESS RANGE

From Value	To Value	Count in Range	% of Total Count
0	0.1	130,061	8.07
0.1	0.2	212,090	13.16
0.2	0.3	361,813	22.46
0.3	0.4	450,797	27.98
0.4	0.5	245,484	15.24
0.5	0.6	130,762	8.12
0.6	0.7	62,327	3.87
0.7	0.8	17,710	1.10
Total		1,611,044	100.00

Due to the size of the domain of solution, 13% of cells had a skewness of over 0.5, as shown in Table 4, which is acceptable. The maximum skewness observed in the mesh was reported as 0.79.

4.2.3 Solution Procedure

The filtered Navier-Stokes equations used by FLUENT in the LES solution follow:

$$\text{---} \quad \text{---} \quad (2)$$

and

$$\text{---} \quad \text{---} \quad \text{---} \quad \text{---} \quad \text{---} \quad (3)$$

where the stress tensor σ_{ij} is

$$\text{---} \quad \text{---} \quad \text{---} \quad \text{---} \quad (4)$$

and τ_{ij} is

$$(5)$$

While using the LES scheme, the Smagorinsky-Lilly model was used as a subgrid scale model. The eddy-viscosity was modeled as

$$(6)$$

where L_S is the mixing length for the subgrid scales

$$(7)$$

and

$$(8)$$

Since the model was an LES, it was decided that the time step would be reduced to 10^{-7} s from 10^{-6} s, as in the previous case. The model was first computed to steady state using the SA model and subsequently executed on the HiPECC at Wichita State University using LES with a time of 0.1 s.

4.2.4 Results

Figure 18 and Figure 19 show the contours of static pressure at 0.05 s, and 0.1 s, respectively.

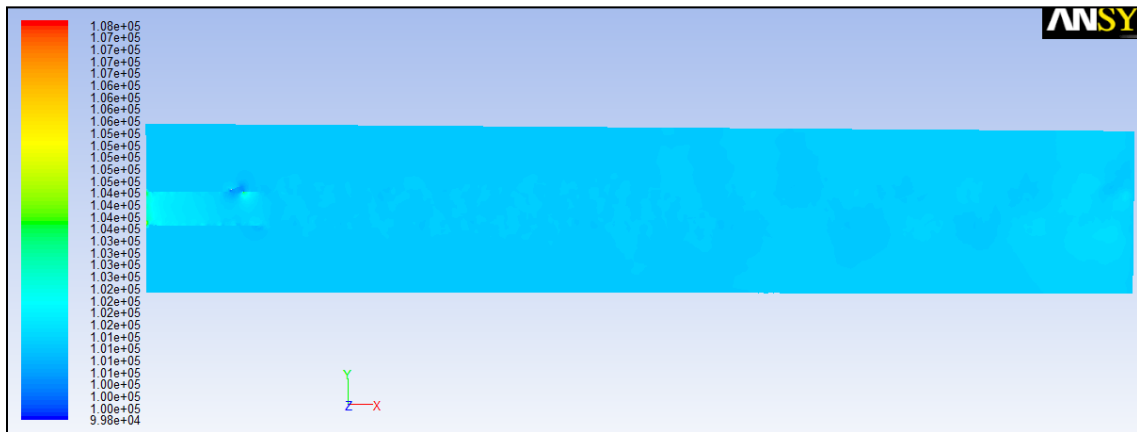


Figure 18. Version 2: Contours of static pressure at 0.05 s

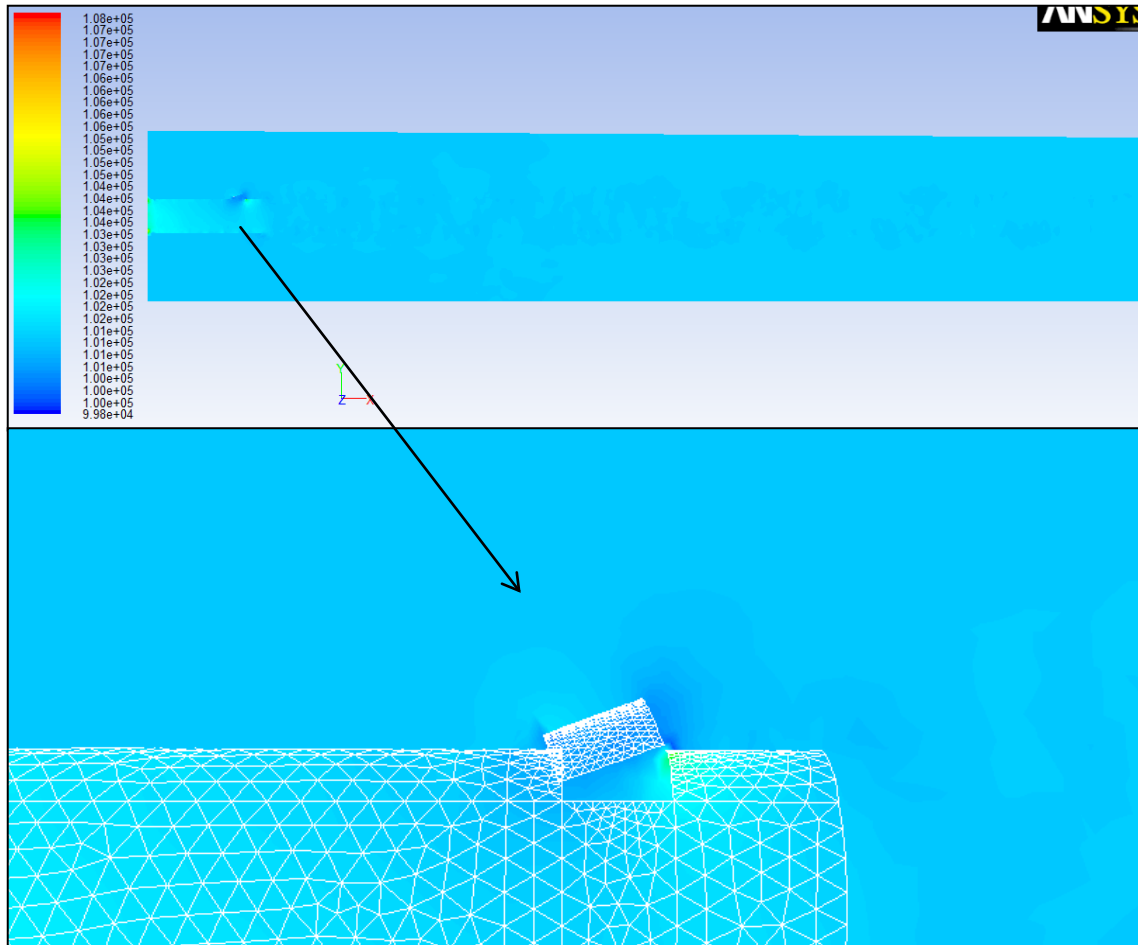


Figure 19. Version 2: Contours of static pressure at 0.1 s

Even though the downstream pressure fluctuations were captured well, the pressure fluctuations around the hatch and opening were not captured nearly as well as expected. The pressure contours showed the region around the hatch where the flow slows down and accelerates relatively well, but could possibly be achieved better with the presence of a boundary layer on the wall surfaces of the internal jet cylinder and hatch. Centerline pressure results are shown along with the results acquired in the final version in the following section.

Figure 20 and Figure 21 show the velocity profiles in the new subsonic test case at the same time steps as that of pressure. The zoomed-in section illustrates the velocity around the

hatch and shows how the freestream velocity slows down due to the presence of a hatch and then mingles with the flow inside the pipe before speeding up.

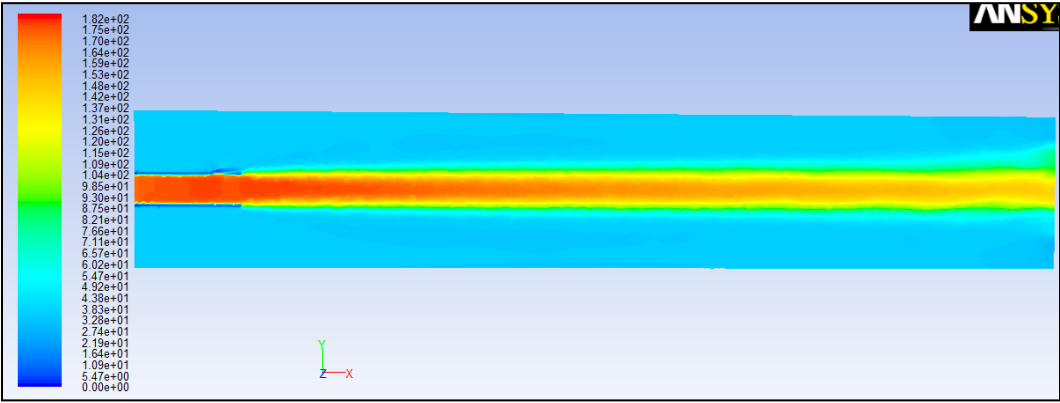


Figure 20. Version 2: Velocity profile at 0.05 s

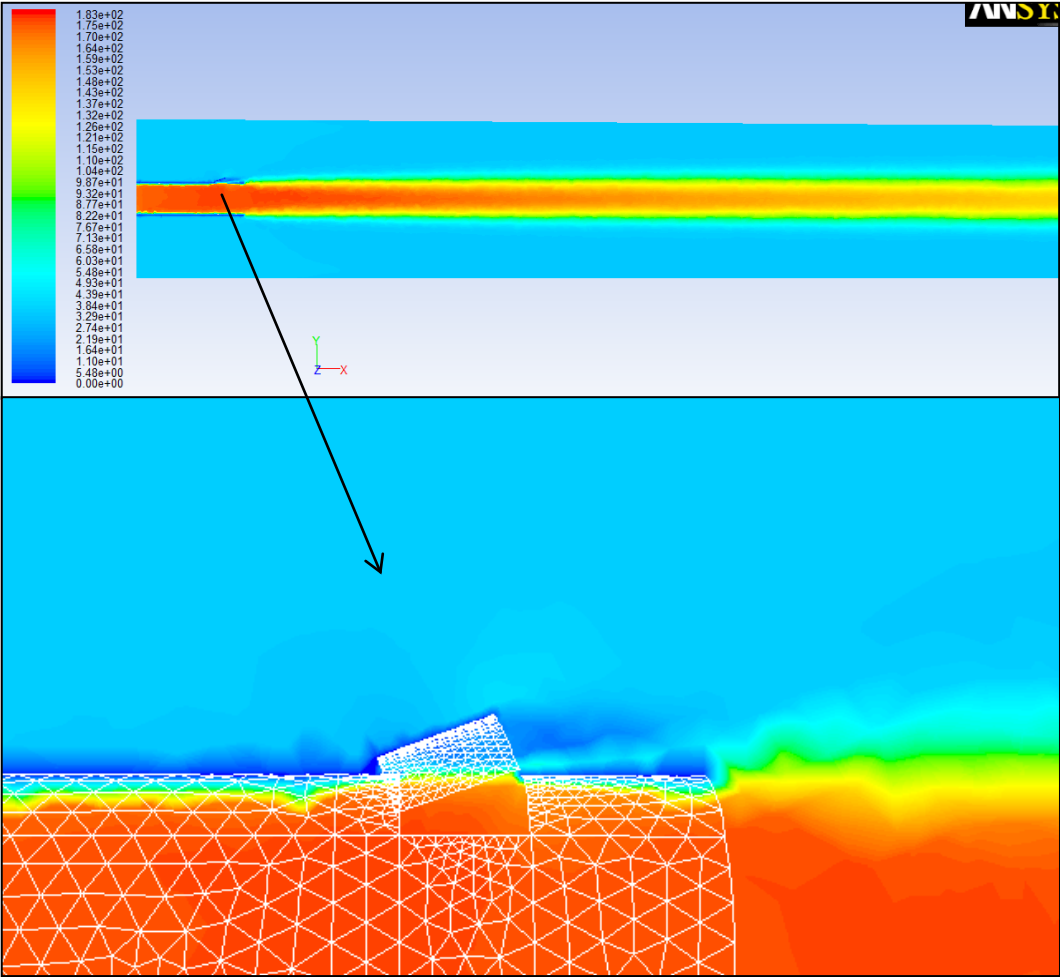


Figure 21. Version 2: Velocity profile at 0.1 s

As can be seen, little visible interaction occurs between the internal jet flow and the external flow under the hatch. In order to obtain a better idea of the aforementioned interactions and to further understand the flow under the hatch, the x-velocity data is represented using TecPlot iso-surfaces at the same time steps as that of the contours. As shown in Figure 22 and Figure 23, the dark-blue region depicts negative x-velocity, and the teal shows a region of 40 m/s. These figures conclusively show that there is mingling flow and rotational flow under the hatch, as expected. It can also be observed that not much change is experienced in the x-velocity under the hatch over the course of the simulation.

X-velocity profiles at $x/D = 2.5, 2.667,$ and 2.833 are shown in Figure 24, and provide a clearer picture of the flow reversal observed under the hatch. Centerline velocity results are shown along with the final version results in the following section.

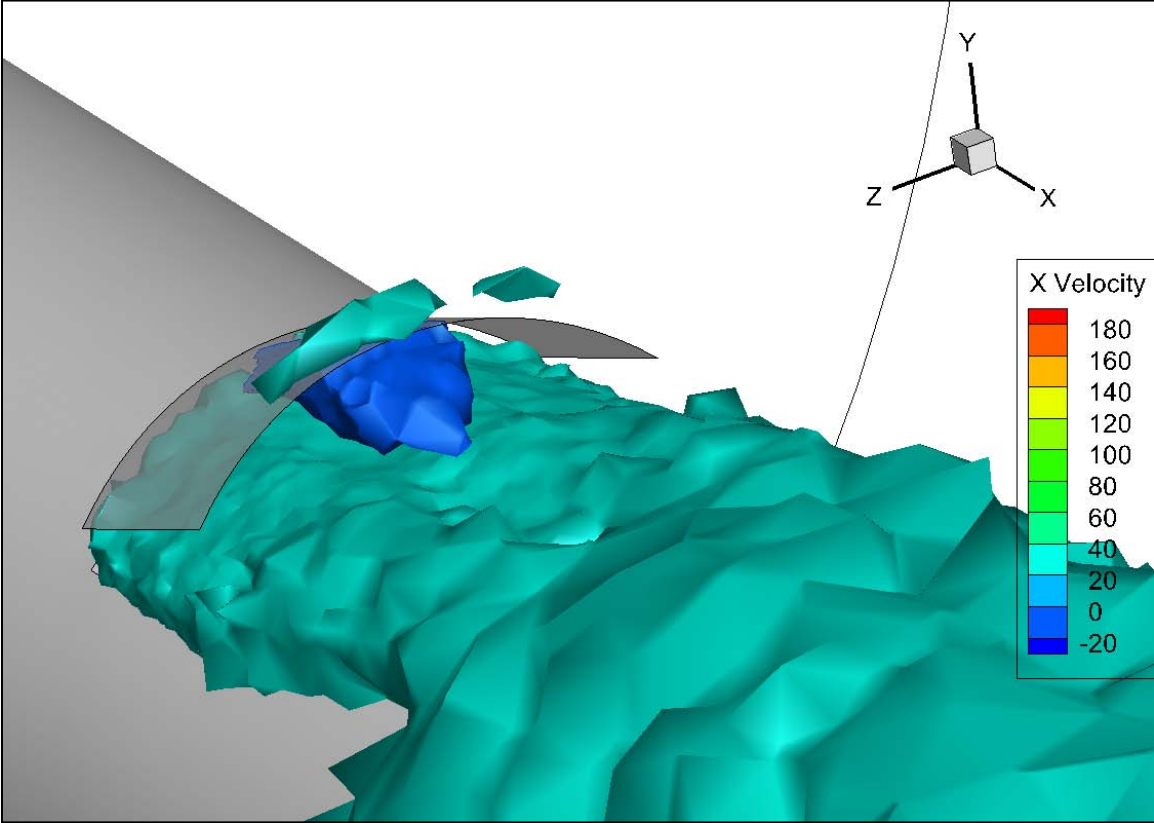


Figure 22. Version 2: X-velocity iso-surface at 0.05 s

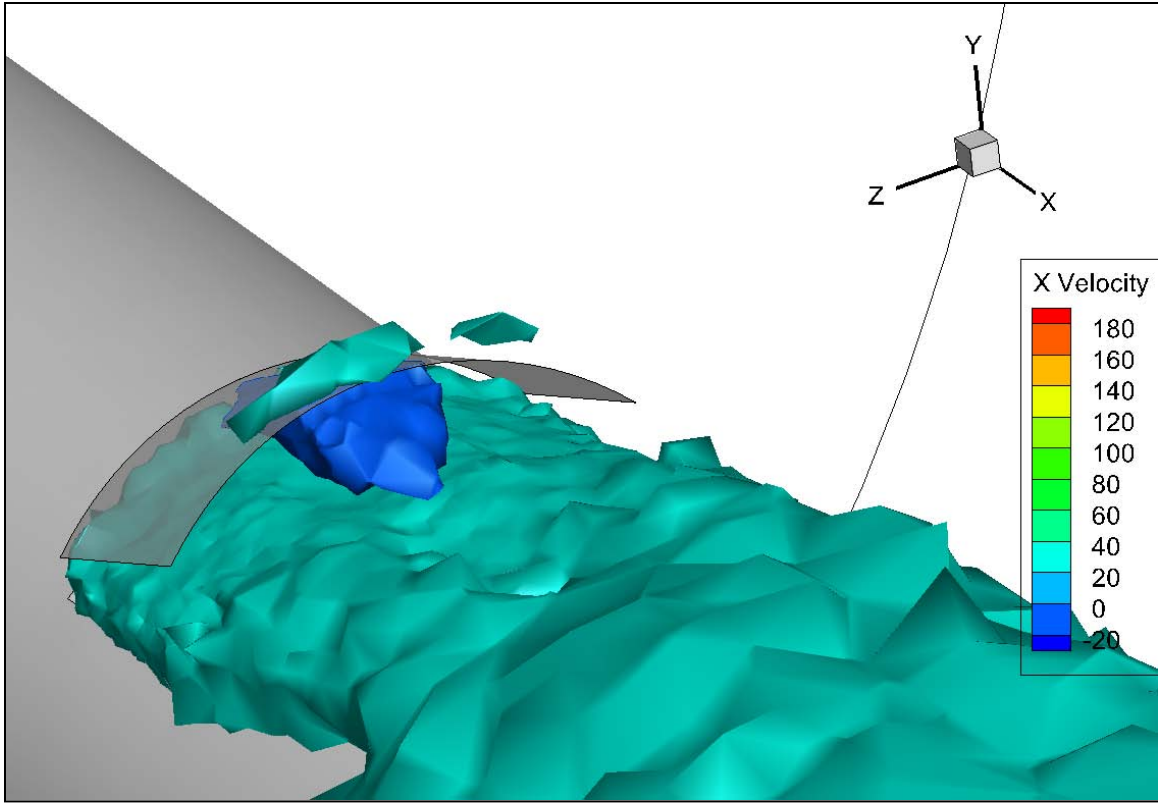


Figure 23. Version 2: X-velocity iso-surface at 0.1 s

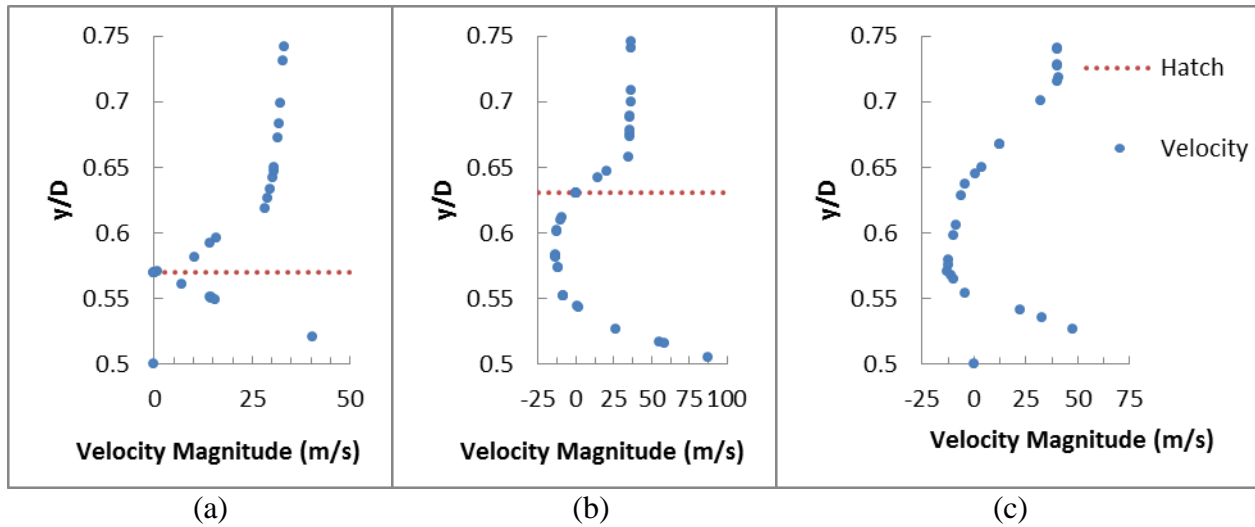


Figure 24. Version 2: X-velocity profiles at (a) $x/D = 2.5$, (b) $x/D = 2.667$, and (c) $x/D = 2.833$

Figure 25 and Figure 26 illustrate turbulent viscosity. No discernible change is observed in the region around the hatch over the course of the simulation. Similar to the contours of static

pressure, it is expected that better resolution will be acquired around the hatch with a greater-density mesh.

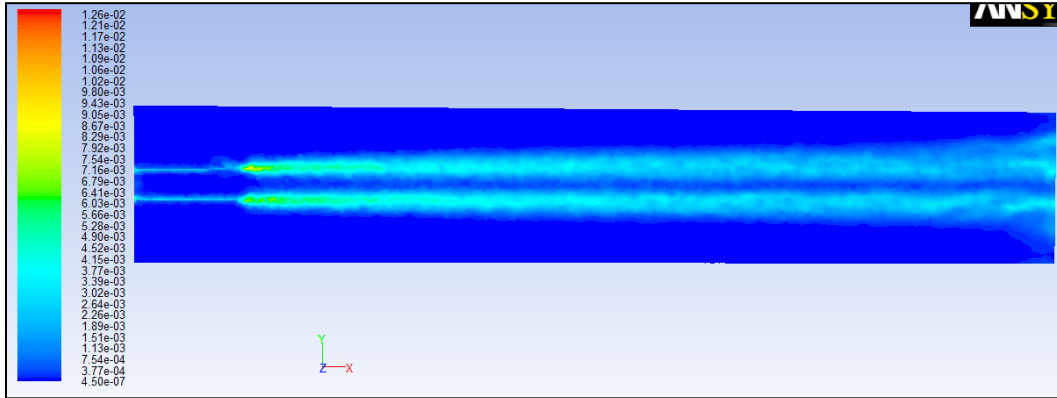


Figure 25. Version 2: Subgrid turbulent viscosity at 0.05 s

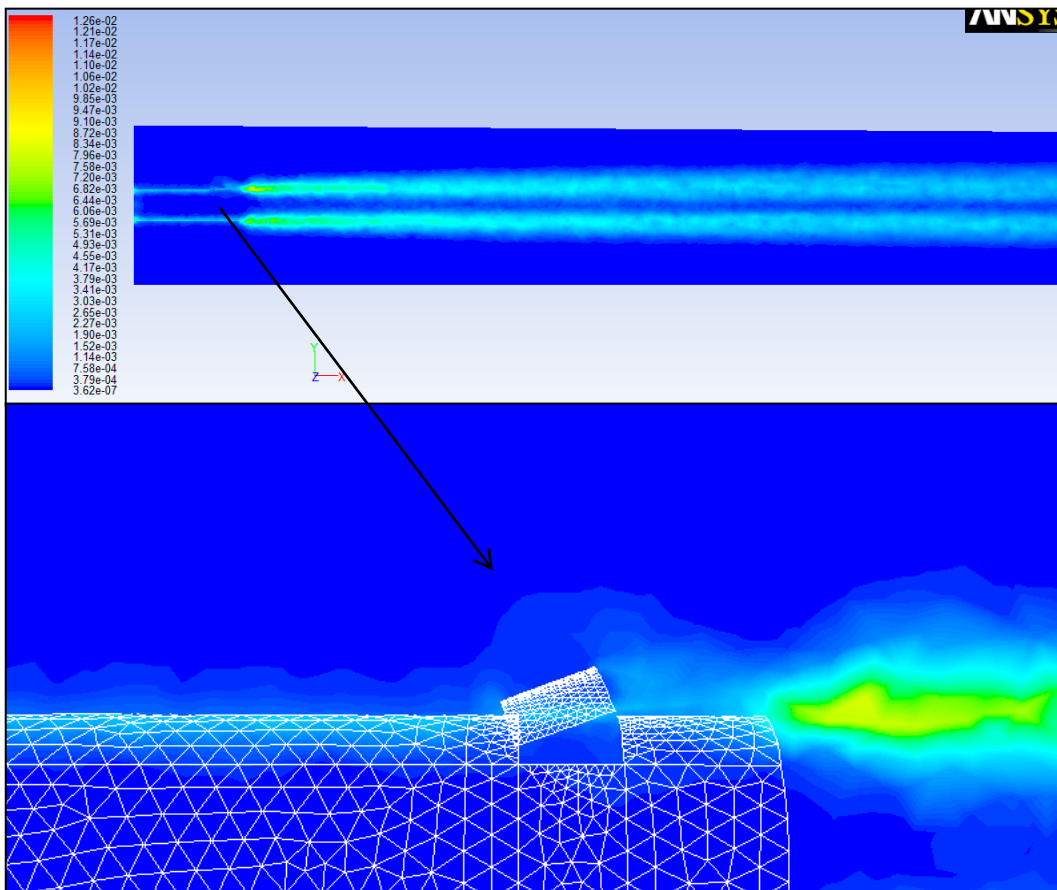


Figure 26. Version 2: Subgrid turbulent viscosity at 0.1 s

Figure 27 shows the location of eight points where static pressure is monitored. Of these, four points are taken “on top” of the hatch, two are taken “below” the hatch, and two are taken “in front” of the hatch.

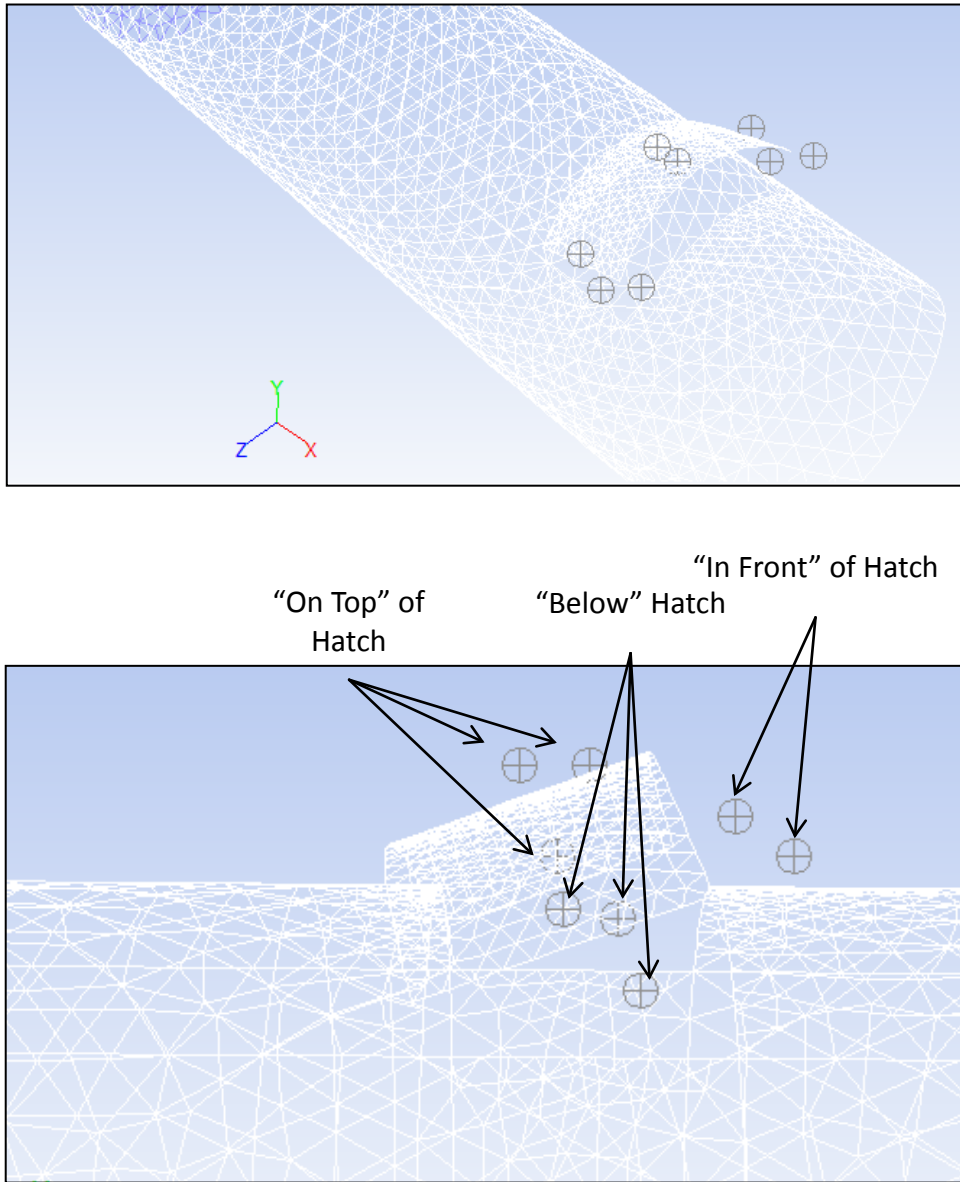


Figure 27. Version 2: Pressure monitors around opening and hatch

Using these points, SPL versus frequency graphs were plotted and are shown in Figures 28 to 30. As far as the range of human hearing is concerned, a general consensus of 20 Hz to

20,000 Hz was reached, and correspondingly, the SPL range was decided at 100 Hz to 20,000 Hz, since sufficient data was not acquired under 100 Hz.

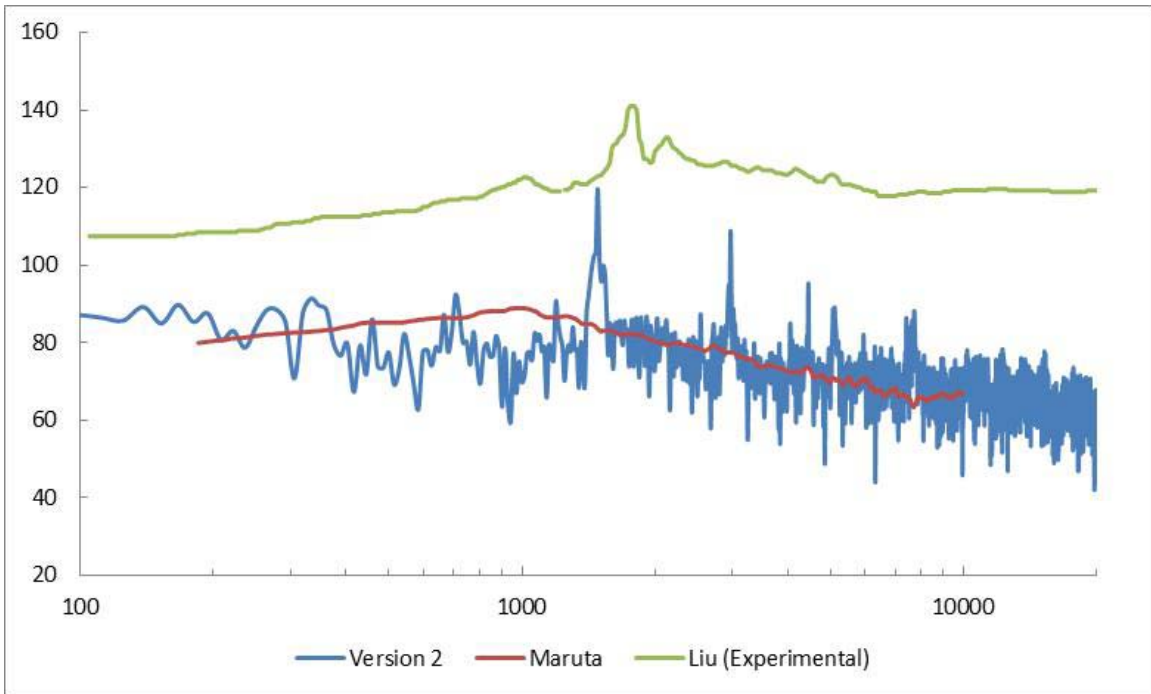


Figure 28. Version 2: SPL “on top” of hatch

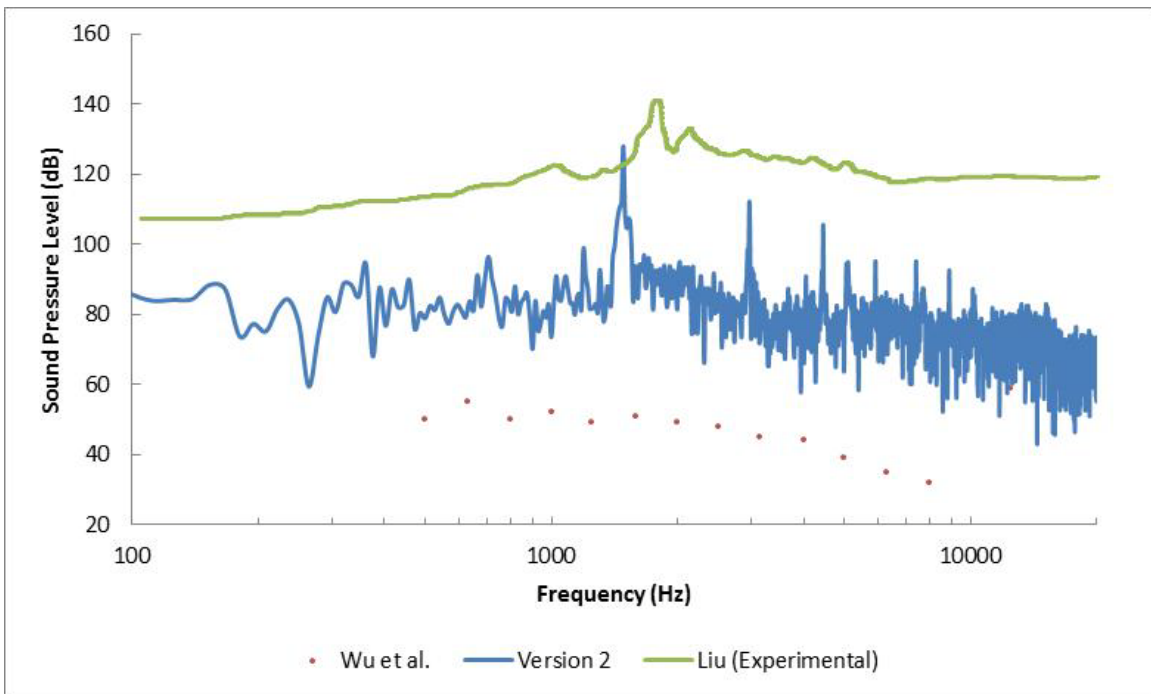


Figure 29. Version 2: SPL “below” hatch

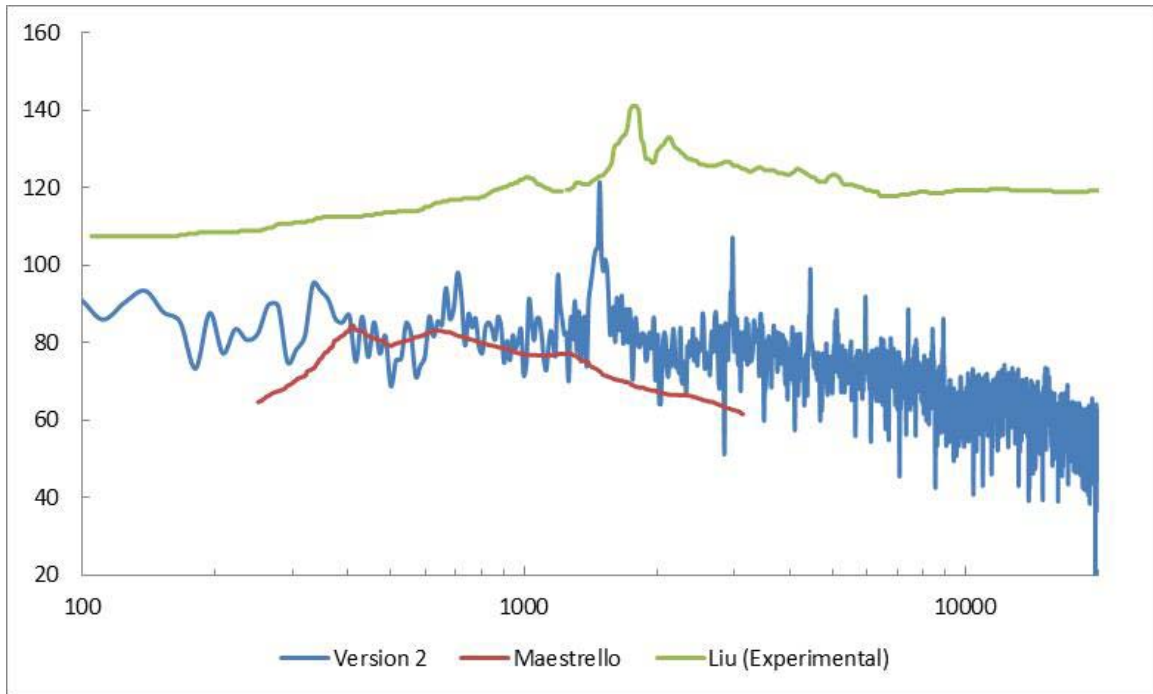


Figure 30. Version 2: SPL “in front” of hatch

Since no experimental data could be found for the geometry being investigated, it was decided to utilize supersonic jet flow data derived from Liu et al. [32] as an upper bound to the tolerable noise level, which is approximately 130 dB. The experiment was conducted at a Mach number of 1.51, and the SPL was gathered 2.2D downstream from the nozzle exit, and 1D above the centerline.

For data acquired “on top” of the hatch, data from Maruta and Kotake [38] was used to compare a sound generated by a flat plate at an angle of 30 degrees, at a Mach number of 0.3. Data was gathered with a microphone stationed behind the plate and was compared to data from the location “on top” of the hatch. It can be seen that the noise observed between the two setups correlates well, especially between 1000 Hz and 10,000 Hz.

Noise generated “below” the hatch was compared to data from Wu et al. [39] who measured noise generated in a cavity at Mach 0.1, along the centerline of the horizontal wall

surface using two flush mounted microphones. Due to the flow being slower in the case of Wu et al., the noise generated was lower than that of Version 2.

Similarly, data acquired from Maestrello's [40] 2mm thick flat plate generated along the centerline in the test section of an open circuit wind tunnel at a Mach number of 0.47 inside the reverberation room was compared to the SPL generated "in front" of the hatch. Good agreement was observed between all three cases and the experimental data.

4.3 Final Version—Unstructured Mesh

4.3.1 Geometry, Domain of Solution, and Boundary Conditions

From the results of Version 2, it was concluded that sufficient data had been collected for downstream velocity and turbulence viscosity profiles. Due to the lack of adequate grid density in the mesh that encompasses the hatch and the opening, while keeping in mind the computation time and power required, it was decided that the domain of solution would be reduced to a length of $x/D = 10$, while retaining the boundary conditions and flow conditions of Version 2. The changes in the domain of solution can be seen in Figure 31.

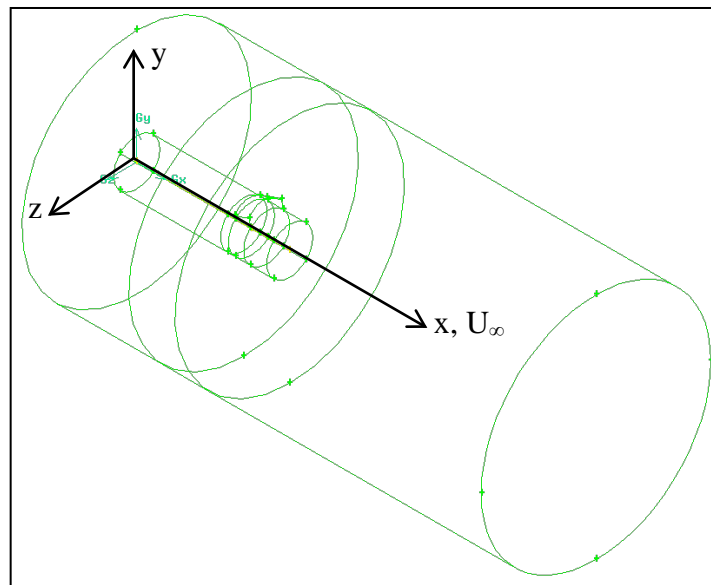


Figure 31. Final Version: Domain of solution

4.3.2 Meshing

As mentioned in section 4.3.1, the objective of this version was to collect better data around the hatch and opening, in order to better understand the phenomenon occurring in that region. To that effect, the cell density in the pertinent volumes was further increased. The goal was to have a dense mesh to effectively capture pressure fluctuations in the region around the hatch and opening, in order to obtain more accurate SPL results.

To present a better understanding of the cell distribution, Table 5 and Table 6 provide a breakdown of the same, using volumes and skewness range as distinguishing criteria. As shown in Table 5, the hatch has a much better cell density compared to Version 2.

TABLE 5

FINAL VERSION CELL DISTRIBUTION—VOLUME

Volume	Number of Cells in Volume
Internal Cylinder	54,079
Hatch	38,420
Region around Hatch	519,145
Rest of Domain of Solution	575,116
Total	1,186,760

TABLE 6

FINAL VERSION CELL DISTRIBUTION—SKEWNESS RANGE

From Value	To Value	Count in Range	% of Total Count
0	0.1	98,272	8.25
0.1	0.2	164,090	13.83
0.2	0.3	277,563	23.39
0.3	0.4	320,869	27.04
0.4	0.5	180,683	15.22
0.5	0.6	92,595	7.80
0.6	0.7	43,762	3.69
0.7	0.8	8,926	0.75
Total		1,186,760	100.00

Due to the size of the domain of solution, 12.5% of cells have a skewness of over 0.5, of which only 0.75% is over 0.7. The maximum skewness observed in the mesh is 0.795, which is also an acceptable value in an unstructured mesh.

4.5.3 Solution Procedure

The solution procedure used is identical to that of Version 2 except that the FLUENT software was updated to the latest version. Just prior to the initialization of the simulation, HiPeCC was updated, and FLUENT V13 was installed on the cluster. The mesh was exported to FLUENT V13, where it was first converged to steady state and subsequently marched in time using the same LES model conditions from the previous version. The time step was also maintained at 10^{-7} s, and the solution was computed till 0.1 s.

4.3.4 Results

Upon completion of the simulation, the following results were acquired. Figure 32 shows the contour of static pressure at 0.1 s. It can be observed that there is conformity in the results observed from the test case in Version 2.

These images also show that there is some minor corruption in data at the inlet. It was discovered that this is caused by “flow reversal at the inlet,” probably due to the interaction of a high density of cells in the “pressure inlet” configuration with cells in the “farfield” configuration. This error has not been observed to propagate any further than the cells at the inlet and has not corrupted the data at the hatch in any way. This phenomenon has been observed in the subgrid turbulent viscosity data to a similar effect.

Figure 32 illustrates the contours of static pressure at 0.1 s, and Figure 33 compares the pressure observed in Version 2 and the Final Version at the centerline. Good agreement is

witnessed between the two test cases, and shows that there is no significant variation on the centerline pressure and that no erratic jumps in pressure occur due to the presence of a hatch.

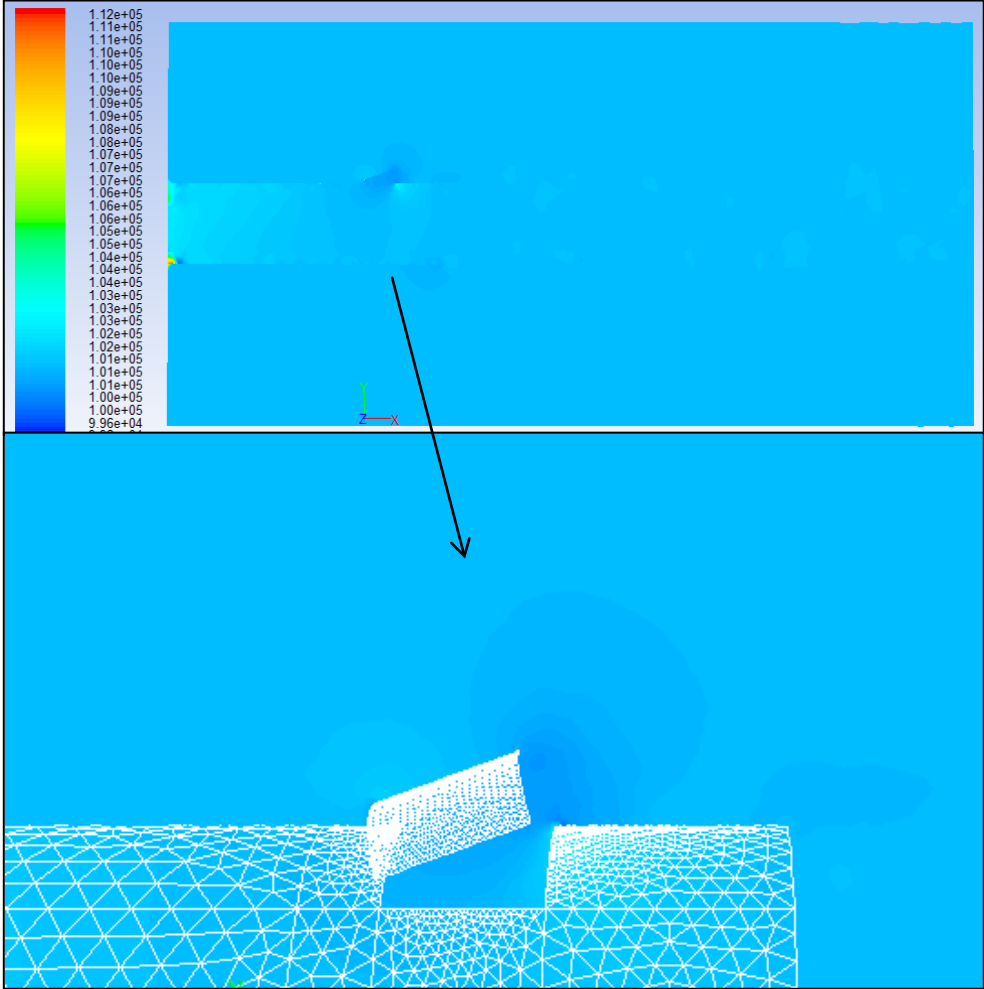


Figure 32. Final Version: Contour of static pressure at 0.1 s

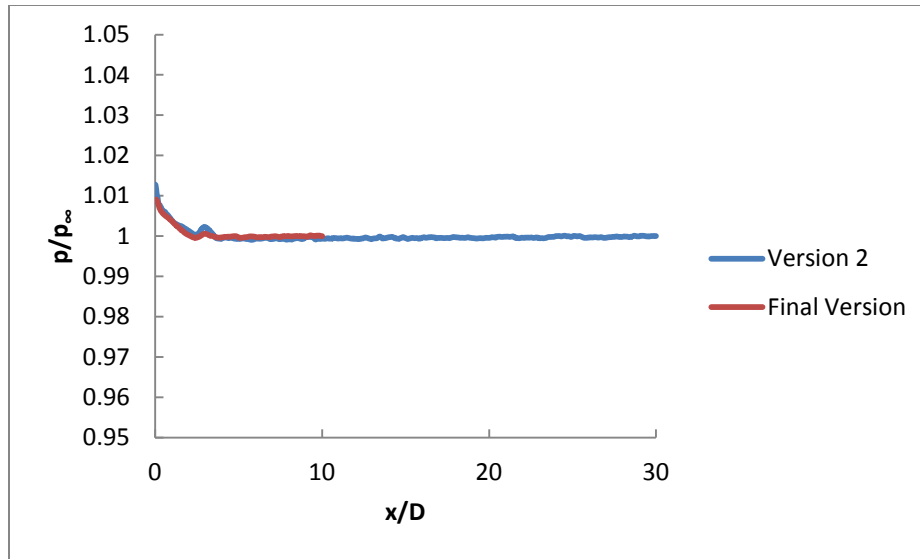


Figure 33. Comparison of centerline pressure at 0.1 s

Figure 34 depicts the magnitude of velocity around the hatch at 0.1 s. It can be seen that the velocity magnitude profile is in good agreement with that of Version 2.

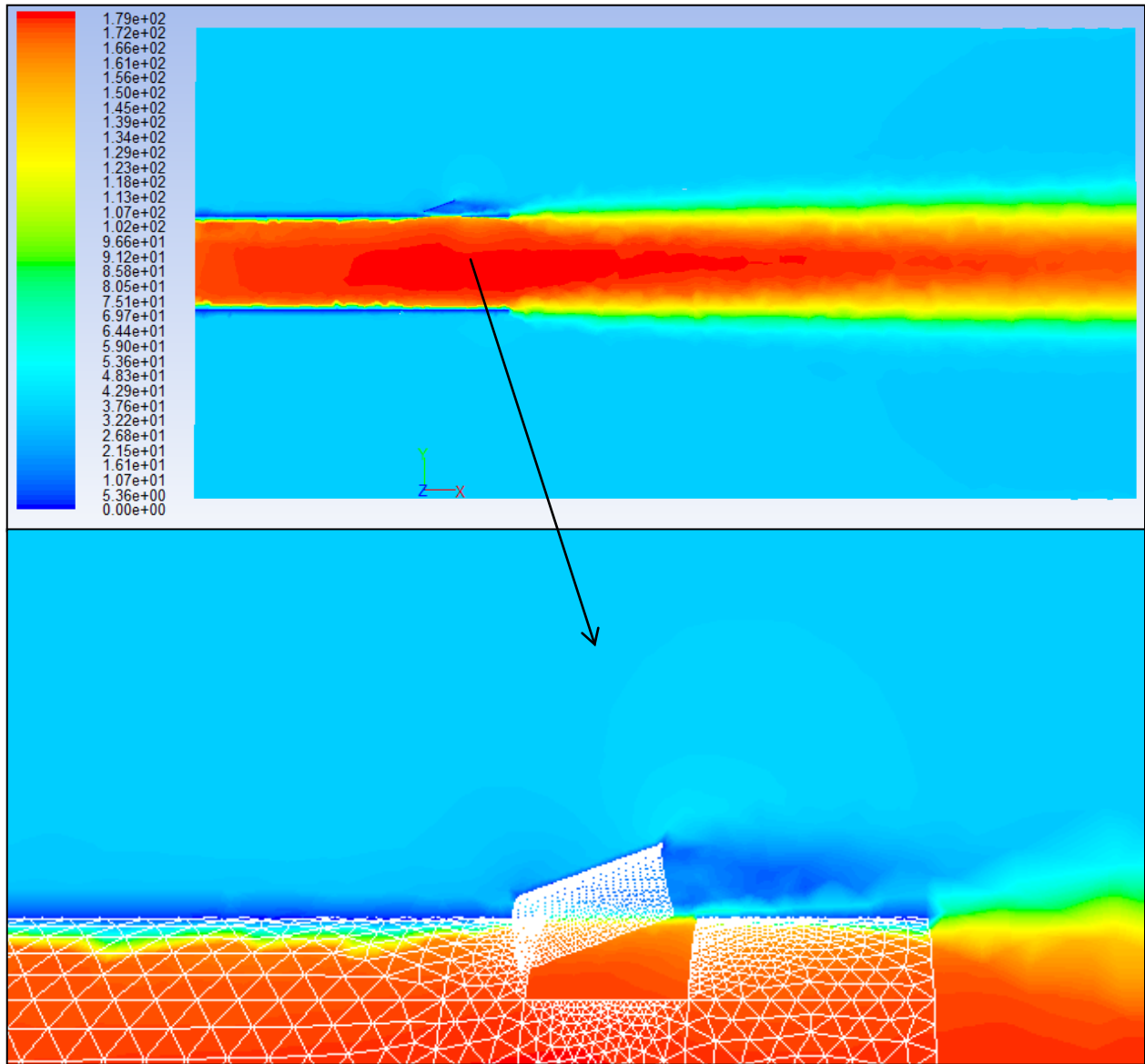


Figure 34. Final Version: Velocity magnitude at 0.1 s

Figure 35 shows the x-velocity iso-surface at 0.1 s. Compared to Version 2, the iso-surface has a greater region with reversed flow as well as a larger region with decelerated flow, due to the increased cell density in that region. To investigate further, Figure 36 shows x-velocity profiles at three locations: $x/D = 2.5$, 2.667 , and 2.833 . As can be seen, reversed flow is observed under the hatch. Data from the two versions are compared and shown to be in good agreement with one another.

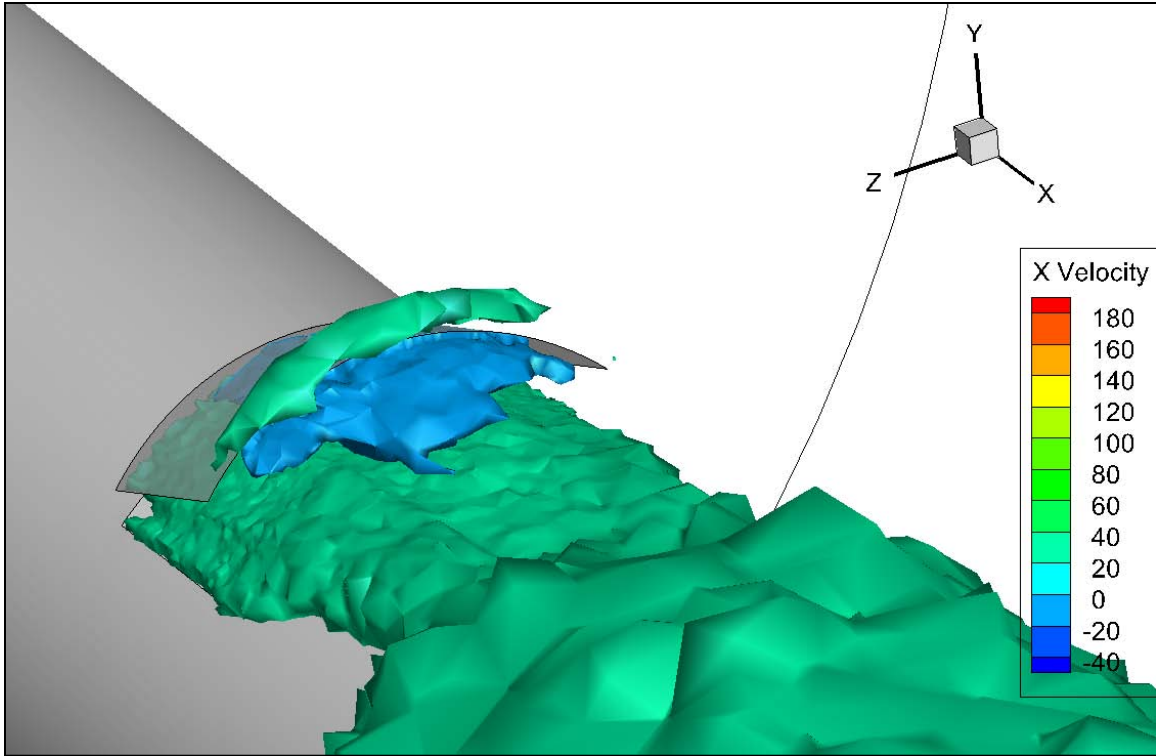


Figure 35. Final Version: X-velocity iso-surface at 0.1 s

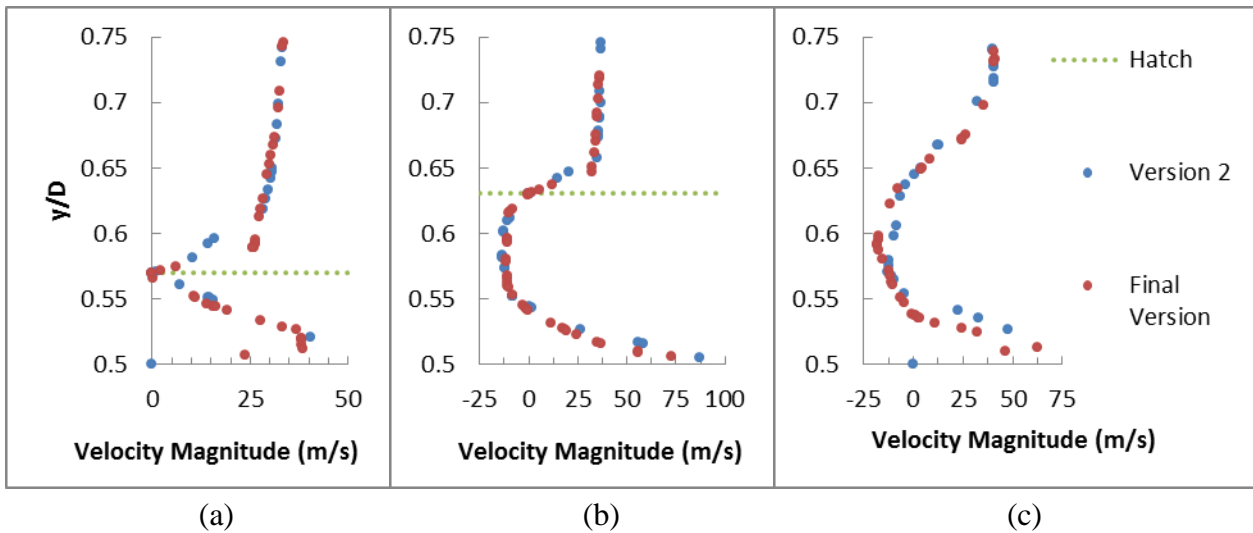


Figure 36. Final Version: X-velocity profiles at (a) $x/D = 2.5$, (b) $x/D = 2.667$, and (c) $x/D = 2.833$

Figure 37 compares the velocity magnitude along the centerline of Version 2 with the Final Version. There is good agreement between the two, and reducing the length of domain of solution from $x/D = 30$ to $x/D = 10$ has no discernible drawbacks.

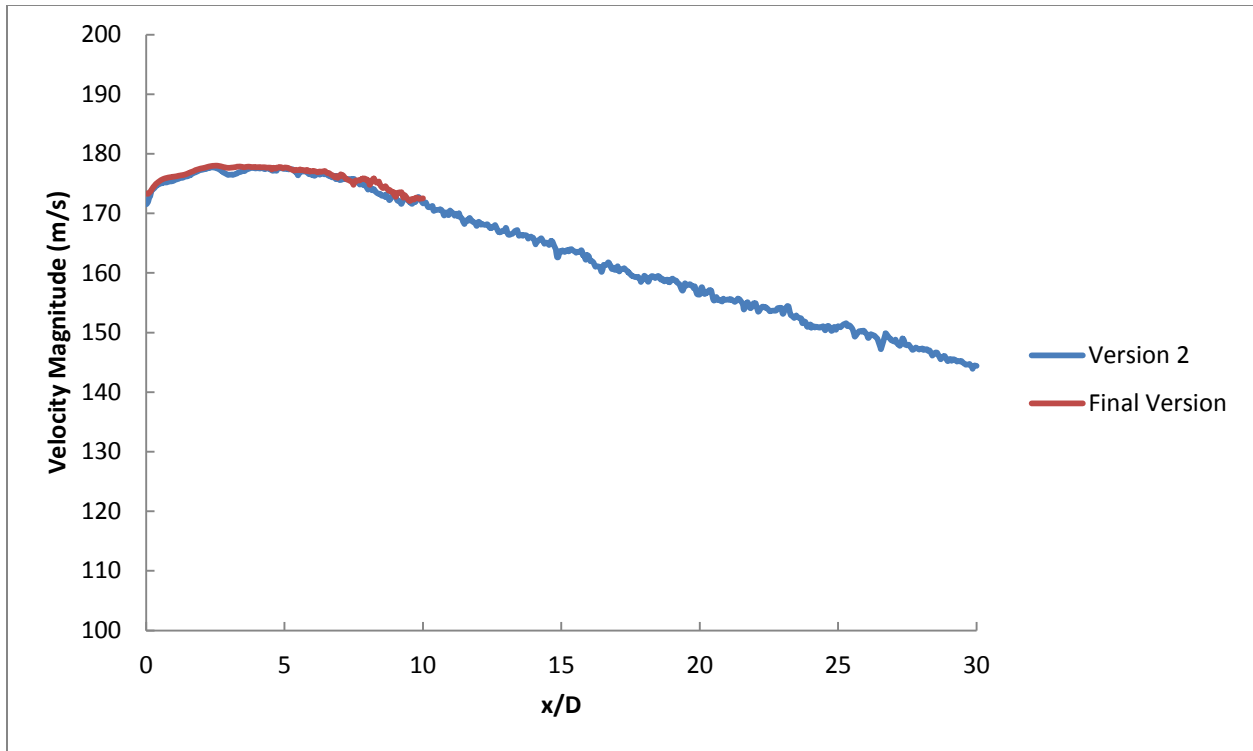


Figure 37. Comparison of centerline velocity magnitude at 0.1 s

Figure 38 shows the subgrid turbulence viscosity at 0.1 s. Results match well with that acquired from Version 2.

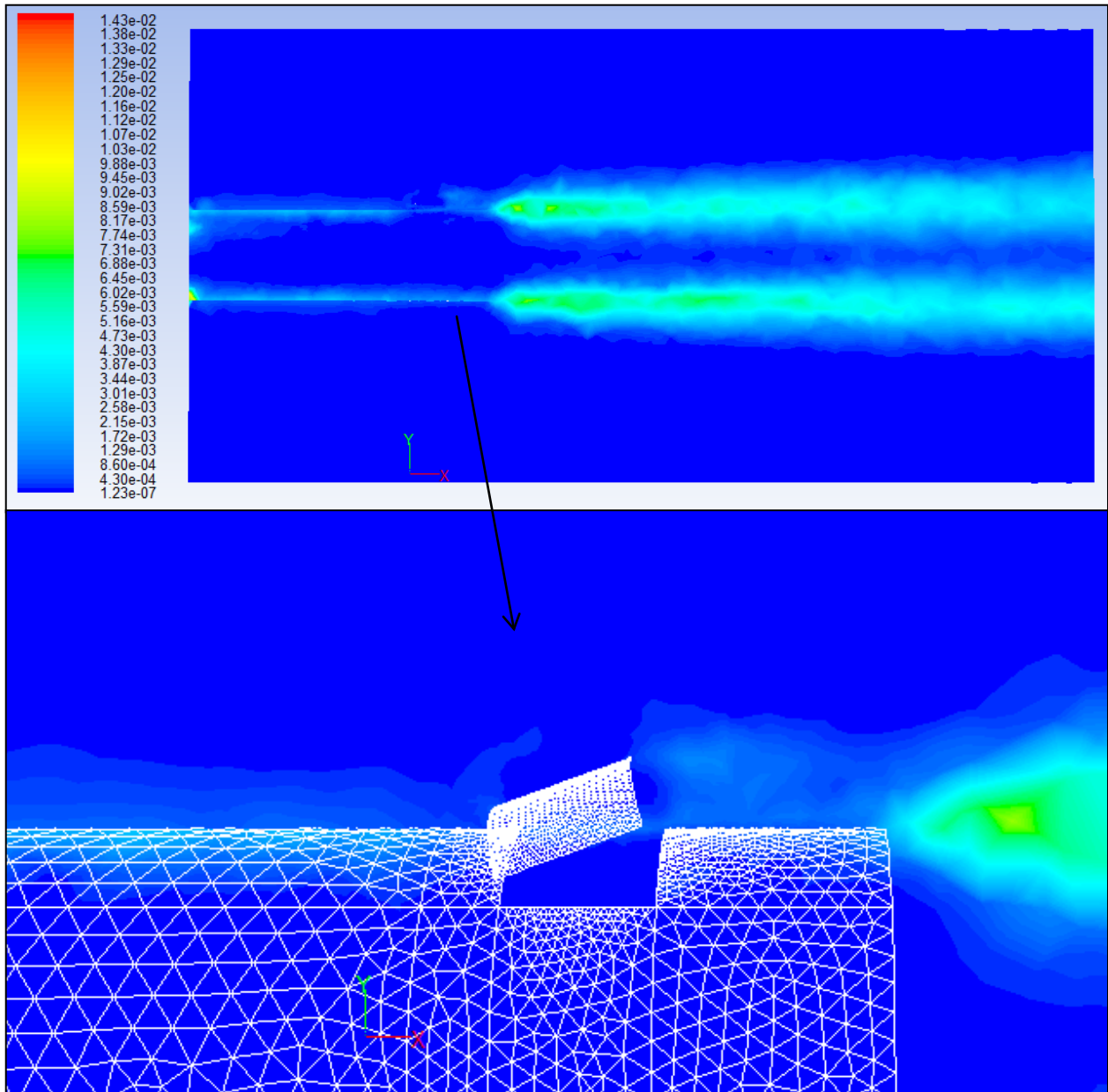


Figure 38. Final Version: Subgrid turbulence viscosity at 0.1 s

In the Final Version, only six static pressure monitors were utilized, as compared to 8 in Version 2. It was noticed that the symmetric locations produced similar pressure data due to the symmetry of the geometry, and hence it was deemed unnecessary to collect the same data twice. Figure 39 shows the changes made.

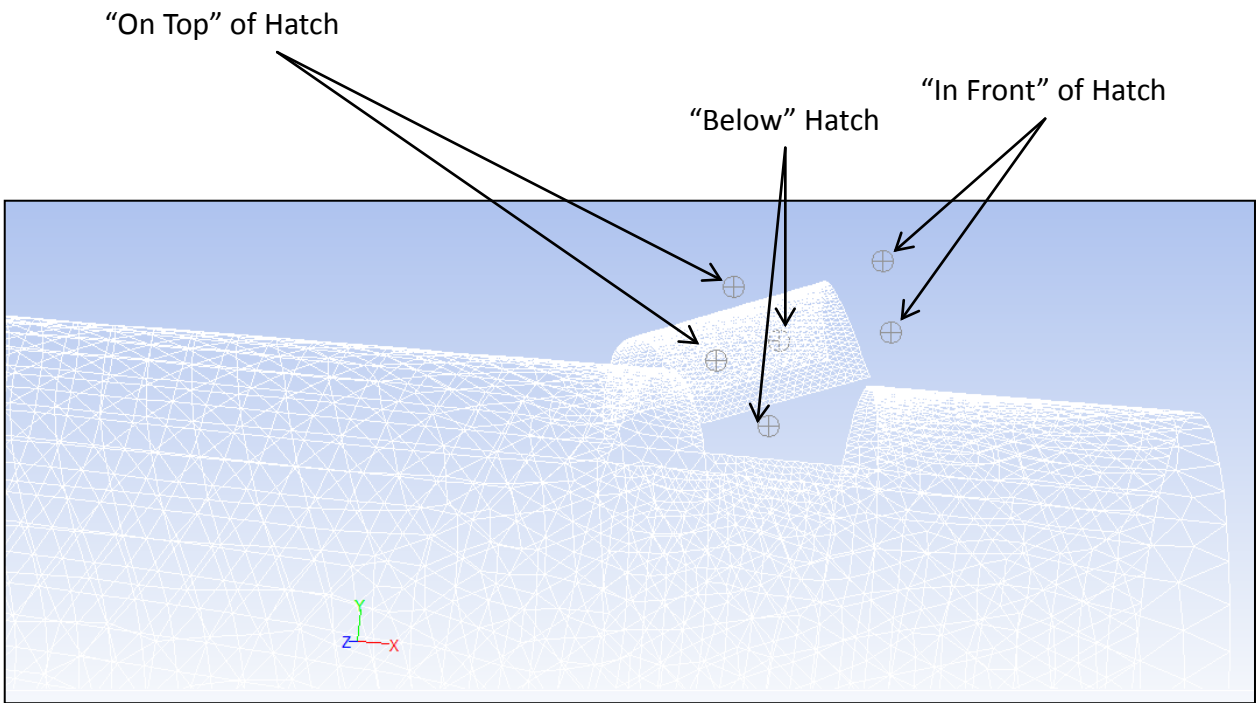
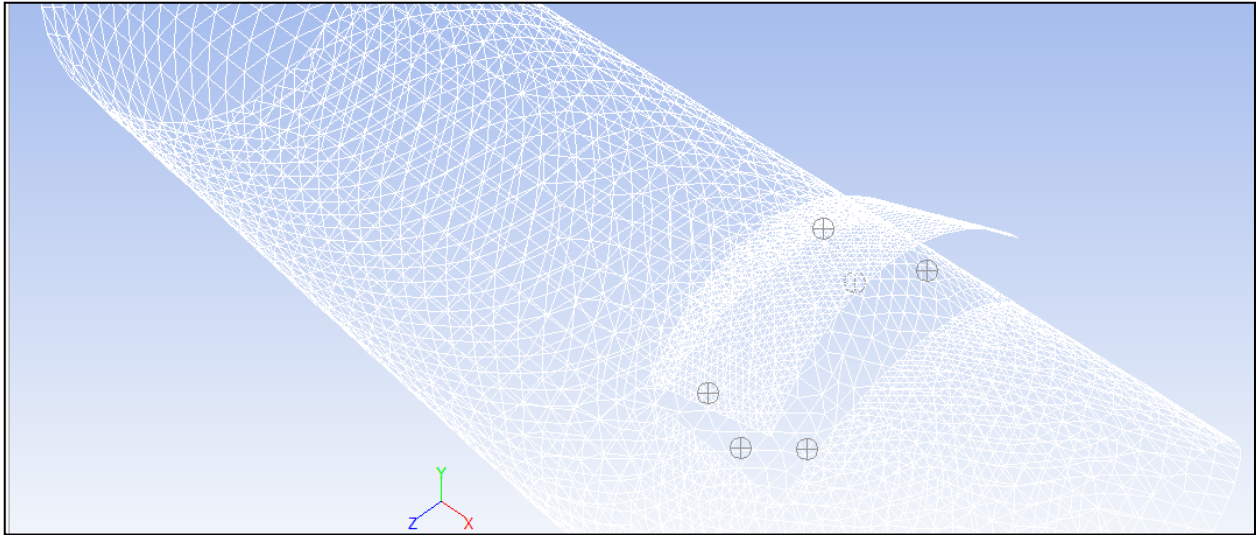


Figure 39. Final Version: Pressure monitors around opening and hatch

Figures 40 to 42 show SPL data collected from “below,” “in front,” and “on top” of the hatch, and it can be seen that the data gathered is consistent with that of Version 2.

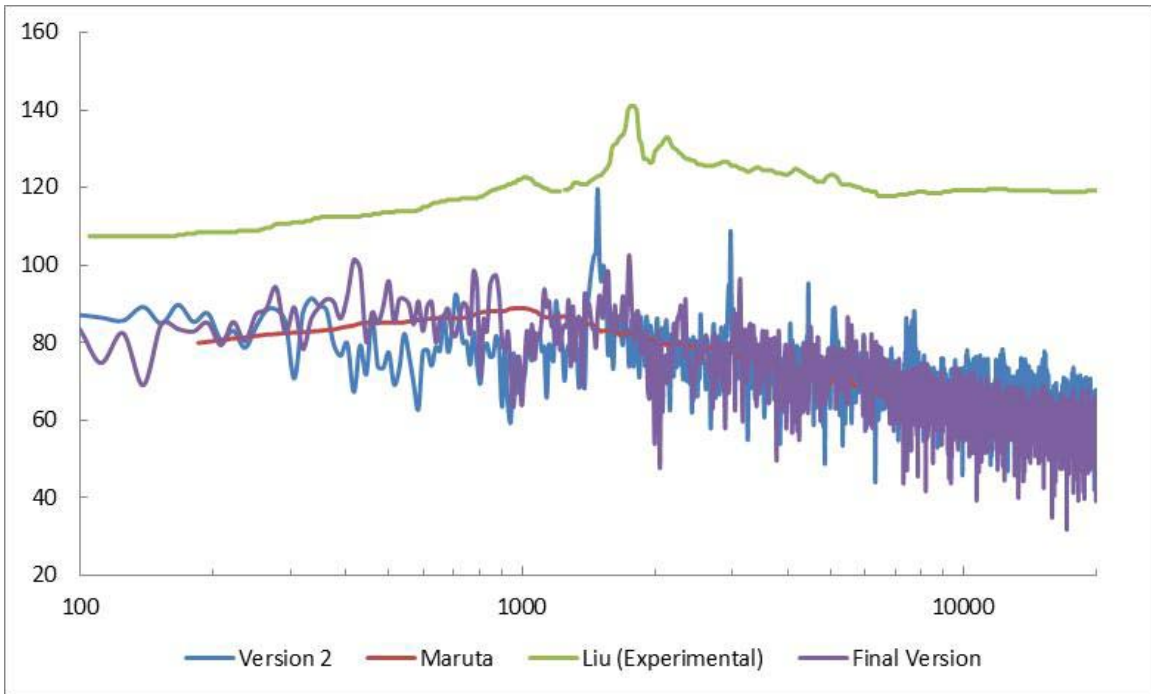


Figure 40. Final Version: SPL “on top” of hatch

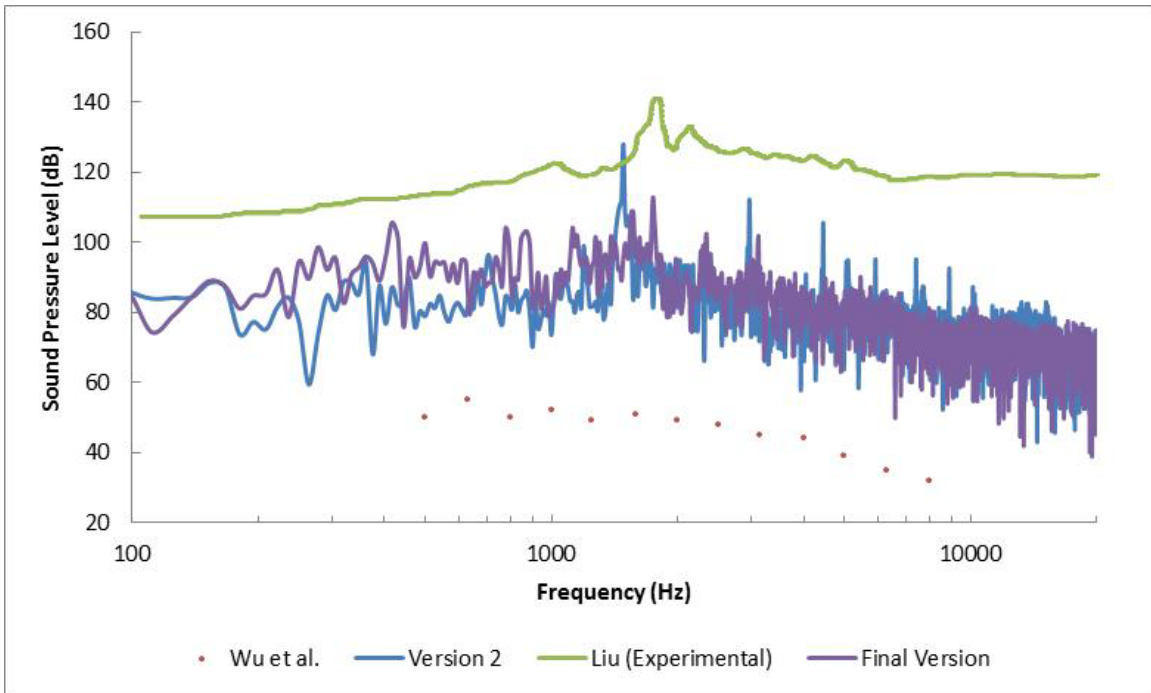


Figure 41. Final Version: SPL “below” hatch

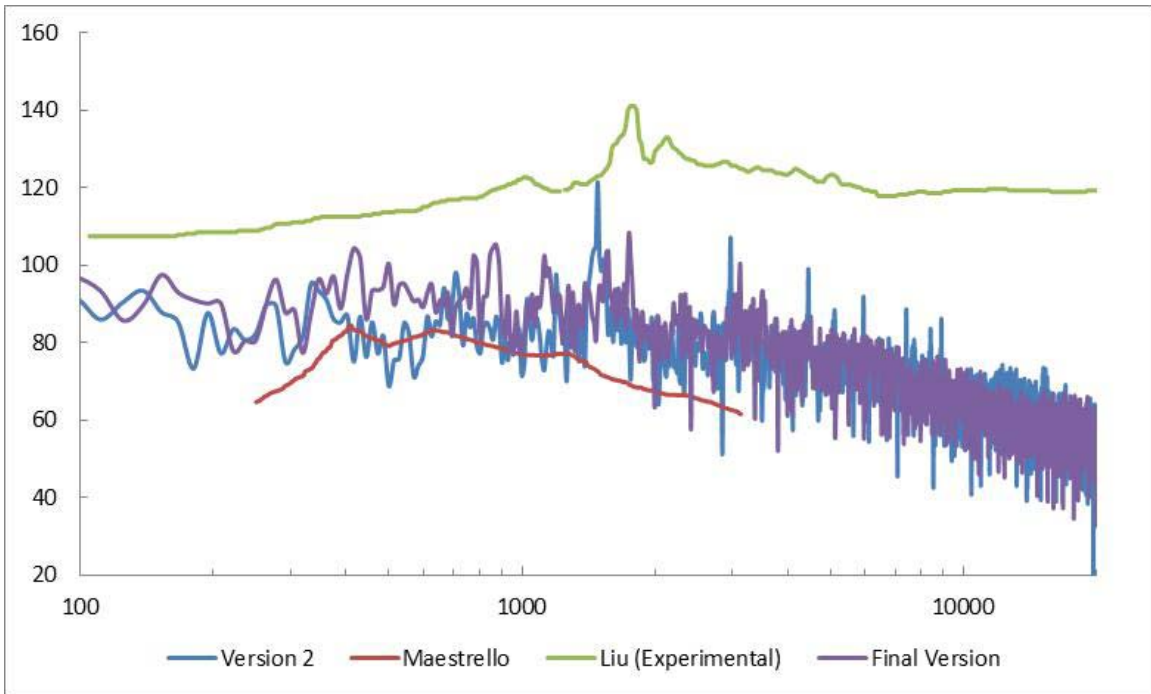


Figure 42. Final Version: SPL “in front” of hatch

CHAPTER 5

CONCLUSIONS

Jet flows through a pipe with an opening and a hatch were numerically investigated in this thesis. Both supersonic and subsonic flows were considered. Upon validating the geometry and boundary conditions using experimental data as well as numerical results reported in the literature, a simulation with supersonic boundary conditions was executed using HiPeCC at Mach 1.4 using a RANS-SA scheme. Results showed the formation of compression waves at the opening as well as exit of the jet pipe. Reversed flow was observed under the hatch, and cross-sectional velocities were presented.

Using the same jet geometry, several domains of solutions of various sizes were specified, and solutions were obtained by an LES scheme for a subsonic flow at Mach number of 0.5. Results of pressure, velocity, and turbulence data gathered in the process were analyzed and compared. Using the pressure data acquired from the simulations, Sound Pressure Levels around the hatch were calculated and compared to various experimental results. Good agreement was seen between data acquired from the two cases on all fronts.

REFERENCES

REFERENCES

- [1] Bull, M. K., “Wall-pressure fluctuations beneath turbulent boundary layers: Some reflections on forty years of research,” *Journal of Sound and Vibration*, Vol. 190, No. 3, 1996, pp. 299–315.
- [2] Willmarth, W. W., “Pressure fluctuations beneath turbulent boundary layers,” *Annual Review of Fluid Mechanics*, Vol. 7, 1975, pp. 13–38.
- [3] Ffowcs-Williams, J. E., “Boundary-layer pressures and the Corcos model: A development to incorporate low-wavenumber constraints,” *Journal of Fluid Mechanics*, Vol. 125, 1982, pp. 9–25.
- [4] Birgersson, F. “Measurements of Structural Response to Turbulent Boundary Layer Excitation: A Review,” TRITA-FKT report, 2001.
- [5] Willmarth, W. W., and Wooldridge, C. E., “Measurements of the fluctuating pressure at the wall beneath a thick turbulent boundary layer,” *Journal of Fluid Mechanics*, Vol. 14, 1962, pp. 187–210.
- [6] Willmarth, W. W., and Roos, F. W., “Resolution and structure of the wall pressure field beneath a turbulent boundary layer,” *Journal of Fluid Mechanics*, Vol. 22, 1965, pp. 81–94.
- [7] Bull, M. K., “Wall pressure fluctuations associated with subsonic turbulent boundary layer flow,” *Journal of Fluid Mechanics*, Vol. 28, 1967, pp. 719–54.
- [8] Howe, M. S., “The role of surface shear stress fluctuations in the generation of boundary layer noise,” *Journal of Sound and Vibration*, Vol. 65, No. 2, 1979, pp. 159–64.
- [9] Goody, M. C., “Empirical spectral model of surface pressure fluctuations,” *AIAA Journal*, Vol. 42, No. 9, 2004, pp. 1788–794.
- [10] Howe, M. S., *Acoustics of Fluid-Structure Interactions*, Cambridge University Press, Cambridge, England, U.K. 1998, p. 208.
- [11] Chase, D. M., “Modeling the wavefactor-frequency spectrum of turbulent boundary layer wall pressure,” *Journal of Sound and Vibration*, Vol. 70, No. 1, 1980, pp. 29–67.
- [12] Goody, M. C., and Simpson, R. L., “Surface pressure fluctuations beneath two- and three-dimensional turbulent boundary layers,” *AIAA Journal*, Vol. 38, 2000, pp. 1822–1831.

REFERENCES (continued)

- [13] Dietiker, J. F., and Hoffmann, K. A., “Predicting wall pressure fluctuation over a backward-facing step using detached-eddy simulation,” *Journal of Aircraft*, Vol. 46, No. 6, 2009, pp. 2155-2120.
- [14] Cobalt, *Cobalt Solutions*, Springfield, Ohio, website URL: <http://www.cobaltcfd.com/index.php/site/software/> [cited Nov. 1, 2011].
- [15] Mahmoudnejad, N., and Hoffmann, K. A., “Numerical computation of wall pressure fluctuations due to a turbulent boundary layer,” 49th AIAA Aerospace Sciences Meeting, Orlando, FL, AIAA Paper No. 2011-1047.
- [16] Lee, Y. T., Farabee, T., and Blake, W. K., “Turbulence effects of wall-pressure fluctuations for reattached flow,” *Journal of Computers and Fluids*, Vol. 38, No. 5, 2009, pp. 1033–1041.
- [17] Bogey, C., and Bailly, C., “Effects of inflow conditions and forcing on subsonic jet flow and noise,” *AIAA Journal*, Vol. 43, No. 5, 2005, pp. 1000–1007.
- [18] Bogey, C., and Bailly, C., “A family of low dispersive and low dissipative explicit schemes for flow and noise computations,” *Journal of Computational Physics*, Vol. 194, No. 1, 2004, pp. 194–214.
- [19] Bogey, C., and Bailly, C., “Three-dimensional non-reflective boundary conditions for acoustic simulations: Far field formulation and validation test cases,” *Acta Acustica*, Vol. 88, No. 4, 2002, pp. 463–471.
- [20] Tinney, C. E., Jordan, P., Delville, J., Hall, A. M., and Glauser, M. N., “A Time-resolved estimate of the turbulence and source mechanisms in a subsonic jet flow,” 44th AIAA Aerospace Sciences Meeting and Exhibit, Reno, U.S.A., AIAA Paper No. 2006-0621.
- [21] Lumley, J. L., “The structure of inhomogeneous turbulent flows,” in *Atmospheric Turbulence and Radio Wave Propagation*, ed. Yaglom and Tatarsky, Nauka, Moscow, 1967.
- [22] Yan, J., Tawackolian, K., Michel, U., and Thiele, F., “Computation of jet noise using a hybrid approach,” 13th AIAA/CEAS Aeroacoustics Conference, 2007, Roma, Italy, AIAA Paper No. 2007-3621.
- [23] Bodnoy, D. J., and Lele, S. K., “Review of the current status of jet noise predictions using large-eddy simulation,” *AIAA Paper 2006-468*.

REFERENCES (continued)

- [24] Ffowcs-Williams, J., and Hawkings, D., “Sound generation by turbulence and surfaces in arbitrary motion,” *Philosophical Transactions of the Royal Society*, Vol. 264, 1969, pp. 321–342.
- [25] Yan, J., Mockett, C., and F. Thiele, F., “Investigation of alternative length scale substitutions in detached-eddy simulation,” *Flow Turbulence and Combustion*, Vol. 74, 2005, pp. 85–102.
- [26] Elzawawy, A., Bravo, L., Andreopoulos, Y., and Watkins, C. B., “Compressibility and density effects in free subsonic jet flows: Three-dimensional PIC measurements of turbulence,” 37th AIAA Fluid Dynamics Conference and Exhibit, Miami, FL, AIAA Paper No. 2007-3858.
- [27] Papamoschou, D., and Roshko, A., “The compressible turbulent shear layer: An experimental study,” *Journal of Fluid Mechanics*, Vol. 197, 1988, pp. 453–477.
- [28] Wang, Z., “Experimental investigation of compressible turbulent jets,” Ph.D. Thesis, City University of New York, 2003.
- [29] Liu, J., Kailasanath, K., Munday, D., and Gutmark, E., “Investigation of near-field acoustic properties of imperfectly expanded jet flows using LES,” 47th AIAA Aerospace Sciences Meeting, 5 Jan 2009, Orlando, FL, AIAA Paper No, 2009-0015.
- [30] Tam, C. K. W., “Jet noise generated by large-scale coherent motion, Aeroacoustics of flight vehicles: Theory and practice,” in *Noise Sources*, ed. H. H. Hubbard, NASA RP-1258, Vol. 1, 1991, pp. 311–390.
- [31] Seiner, J. M., and Yu, J. C., “Acoustic near-field properties associated with broadband shock noise,” *AIAA Journal*, Vol. 22, No. 9, 1984.
- [32] Liu, J., Kailasanath, K., Ramamurthy, R. Munday, D., Gutmark, E., and Lohner, R., “Large-eddy simulation of a supersonic jet and its near-field acoustic properties—Methodology and validation,” 47th AIAA Aerospace Sciences Meeting, Orlando, FL, AIAA Paper No. 2009-0500.
- [33] Dietiker, J. F., and Hoffmann, K. A., “Detached-eddy-simulation of supersonic jet flows,” 6th AIAA Aviation Technology, Integration and Operations Conference (ATIO), September 2006, Wichita, KS.
- [34] Panda, J., and Seasholtz, R. G., “Velocity and temperature measurements in supersonic free jets using spectrally resolved Rayleigh scattering,” NASA TM 2004-212391, 2004.

REFERENCES (continued)

- [35] Fluent, *ANSYS FLUENT Flow Modeling Software*, Canonsburg, Pennsylvania, website URL: <http://www.ansys.com/products/fluid-dynamics/fluent/> [cited Nov. 1, 2011].
- [36] Gambit, *ANSYS-FLUENT Flow Modeling Software*, Canonsburg, Pennsylvania, website URL: <http://www.ansys.com/products/fluid-dynamics/default.asp> [cited Nov. 1, 2011].
- [37] TecPlot Inc., Bellevue, Washington, website URL: <http://www.tecplot.com/> [cited Nov. 1, 2011].
- [38] Maruta, Y., and Kotake, S., “Separated flow noise of a flat plate,” Institute of Space and Aeronautical Science, University of Tokyo, Report No. 592, 1981.
- [39] Wu, S. F., Wu, G., Puskarz, M. M., and Gleason, M. E., “Noise transmission through a vehicle side window due to a turbulent boundary layer excitation,” *Journal of Vibration and Acoustics, Transactions of the ASME*, Vol. 119, 1997, pp. 557-562.
- [40] Maestrello, L., “Measurement of noise radiated by boundary layer excited panels,” *Journal of Sound and Vibration*, Vol. 2, No. 2, 1965, pp. 100-115.